Wave-resolving Voronoi model of Rouse number for sediment entrainment

Johannes Lawen[1]

[1]Hamburg University of Technology, Am Schwarzenberg-Campus 4 (C), Hamburg, 21073, Germany

Correspondence: Johannes Lawen (jl@environment.report)

Abstract. To integrate wave and sediment transport modeling, a computationally extensive wave-resolving Voronoi mesh-based simulation has been developed to improve upon heretofore separate sediment and spectral wave modeling. Orbital wave motion-dependent sediment transport and fine structures of the dynamic Rouse number distribution across the seabed were brought into focus. The entirely parallelized wave-resolving hydrodynamic model is demonstrated for nearshore beach waters adjacent to artificial islands in Doha Bay. The nested model was validated with tidal time series for three locations and two seasons.

1 Introduction

Wave-resolving hydrodynamics, similar to direct numerical simulations (DNS) of turbulent eddy mixing, requires resolutions that are usually impossible or impracticable to compute within even logarithmic orders of the TFLOP range. Therefore, waves and sediment transport have heretofore been simulated separately (Hsu et al., 2005; Anastasiou and Sylaios, 2013; Yu et al., 2018), entailing a principle limit in rigor. This work advances the integration of both into a single finite volume simulation by exploiting that the smallest part of the wavelength spectrum does not transmit to the seabed. That is, wave motion not in contact with the seabed does not need to be resolved to depict entrainment.

Waves modeled herein do, thus, not encompass the entire wavelength spectrum, which would also include short waves that barely perturb shear forcing on the seabed. Therefore, in respect to bottom shear, wave-resolving computation can be attained well before full coastal DNS. Caution is required, as this approach might be valid only for certain wave regimes and climates, and invalid during others that exhibit waves too short to resolve but long enough to be in contact with the seabed.

If conditions are calm, with wind waves exhibiting wavelengths much smaller than twice the water depth, then the perturbation of near-bottom tidal currents due to orbital wave motion remains negligible. If conditions are sufficiently agitated such that wavelengths reach in size the order of magnitude of the water depth, then wave orbital motion may considerably influence bottom currents. High energy waves yield disproportionate increases in erosive fluxes, contributing considerably to shoreline development. Simulating waves and sediment transport in an integrated model, capable of resolving waves, can, thus, enhance accuracy in the depiction of sediment transport.

The sections below contain the wave-resolving simulation of the Rouse number distribution to resolve small scales in the balance of sediment entertainment and deposition. The developed Voronoi model is suitable for wave resolution as the variable

number of edges per finite volume reduces wave fronts on acute triangle angels. In terms of numerical diffusion (Holleman et al., 2013), Voronoi meshes exhibit a reduction compared to Delaunay meshes (Chan et al., 2018). An analytical verification of the model, made tractable by dynamic domain contractions, has been documented separately (Lawen, 2023). Earlier Delaunay versions of the model have been in use for a decade (Lawen et al., 2013, 2014) for studies of reactive transport.

Several reasons might have initially supported the choice of unstructured Delaunay triangle meshes (Lawen et al., 2014) that followed models based on structured meshes (Lawen et al., 2010) vis-á-vis Voronoi meshes: For example, cells in the latter mesh type are formed by a varying number of edges. Absent sparse storage mode, arrays for vertices and faces are in size, thus, determined by the Voronoi cell with the most faces. Meanwhile, triangle cells have always just three horizontal faces (Lawen et al., 2013, 2014; Cousins et al., 2013; Tadesse and Fröhle, 2020), yielding compact arrays for early cache-fitting simulations on multiple bus-snooping and, thus, cache-coherent cores or CPUs. Voronoi meshing has lately also been applied to oceanography, with works (Herzfeld et al., 2020; Ringler et al., 2013) mentioning different stability concerns vs. Delaunay mesh-borne models. That is, an algorithm that might be stable on a Delaunay mesh might not necessarily be stable on a Voronoi mesh.

The need for the developement of ocean models based on Voronoi meshes has been put forth with dedicated emphasis (Ringler et al., 2013): "all 23 global ocean models used in the Intergovernmental Panel on Climate Change (IPCC) 4th Assessment Report (on Climate Change, 2007) were based on structured, conforming quadrilateral meshes (see Chapter 8, pg 597 of Randall and Bony, 2007). Our view is that the global ocean modeling community benefits from having a diversity of numerical approaches. While this diversification is well underway with respect to the modeling of the vertical coordinate (Hallberg, 1997; Bleck, 2002), progress in developing new methods for modeling the horizontal structure of the global ocean on climate-change time scales has lagged behind". The Voronoi mesh-borne model provided herein further contributes to the requested diversity, particularly Voronoi-borne modeling.

Model validation was conducted with five correlations of simulated surface elevations with time series from a tidal survey of three locations and two seasons. In terms of hydrodynamic constituents examined in the validation, reliable validation is frequently relying on time series for surface elevations, as conceded in a number of works (Hsu et al., 1999; Blumberg, 1977; Oey et al., 1985; Park, 1993; Muin and Spaulding, 1996) and found therein as the simulated quantity that exhibits the best correlation with survey measurements. This follows from the magnitudes of the hydrostatic and momentum terms and has been generally observed, including in recent works (Lawen et al., 2013, 2014; Yu et al., 2017). That is, earth's gravity nivellates watertables such that tidal constituents are usually rather well-posed quantities in comparison to velocity components. The bottom drag was calibrated to vertical current profiles to obtain reliable values for bottom roughness.

2 Method

The Cauchy PDE adds the depiction of stresses to the Euler momentum PDE. In the Navier-Stokes PDE the stresses of the Cauchy PDE are specified for Newtonian fluids, that is, molecular momentum dissipation being proportional to the fluid's shear rate. Reynolds-averaged Navier-Stokes (RANS) and large eddy simulations (LES) harness momentum transport by utilizing

the diffusive term in the NS PDE. Approximations and configurations of the latter for coastal ocean domains are known as shallow water PDE or primitive equations, primitive in the sense of fundamental governing function. The model solves, in conjunction with the continuity PDE 10, the incompressible Navier-Stokes PDE 1 configured for surface flow, which accounts in the control volume V (m^3)

$$\frac{\partial(\rho\,\boldsymbol{u}\,V)}{\partial t}+\sum_{n}\frac{\partial\left(u_i\rho_i\,\boldsymbol{u}\,V\right)}{\partial x}=\boldsymbol{F}+\boldsymbol{\nabla}\cdot\begin{pmatrix}\tau_{xx}\tau_{xy}\tau_{xz}\\ \tau_{yx}\tau_{yy}\tau_{yz}\\ \tau_{zx}\tau_{zy}\tau_{zz}\end{pmatrix} \tag{1}$$

for component velocities $\boldsymbol{u}=[u\;v\;w]$ $(\mathrm{m\,s^{-1}})$, with the force $\boldsymbol{F}$ $(\mathrm{kg\,m\,s^{-2}})$ due to the hydroststic pressure gradient and Coriolis acceleration, as explicated in Subsections 2.2 and 2.3. The stress tensor τ_{ij} $(\mathrm{kg\,m^{-1}\,s^{-2}})$ is in Subsection 2.4 configured for an incompressible Netwonian fluid and horizontally isotropic viscosity. The utilization of finite volume approximations is demonstrated for all terms in the subsequent dedicated Subsections 2.1 on continuity, 2.2 on advection and hydrostatic pressure, 2.3 on Coriolis acceleration, 2.4 on viscous stress, 2.5 on the Smagorinsky coefficient computation, 2.6 on hydrodynamic boundary conditions, 2.7 on sediment transport, and 2.7 on erosion. These subsections also incorporate a derivation of the respective terms.

If component velocities are uniform throughout a finite volume, then the latter is termed convective: quantities are uniformly "convected" throughout a cell. If component velocities are nonuniform throughout a finite volume, then an algorithm is termed conservative if the same quantities exit and enter adjacent finite volumes through faces. That is, constituents are conserved and not lost throughout the domain. Variable velocities within one finite volume, that is, the conservative case, correspond to transport velocities remaining in the PDE's derivative. Transport velocities can be arranged outside the PDE's derivative, corresponding to uniform velocity components in a finite volume, if the continuity PDE is inserted into the concerned quantity's PDE. The PDE system is then termed convective.

A uniform velocity is obviously more suitable to warrant constituent emission out of a finite volume. Therefore, conservative algorithms are less likely to ascertain the stability of the simulation, particularly if errors are repetitively amplified in circulations (Lawen et al., 2014). Both cases are here derived via a constituent balance of a finite volume. While considering a convective case of quantity transport, the conservative case is still used to derive the algorithm for the continuity PDE. A control volume balance of quantity flows j_i along x_i (m), for dimension i and quantity f, yields

$$\frac{\partial f}{\partial t}=-\sum_{n}\frac{\partial j_i}{\partial x_i}dx_i \tag{2}$$

for n spatial dimensions. That is, for advection with velocity components u, v, and w $(\mathrm{m\,s^{-1}})$

$$\frac{\partial f}{\partial t}=-\sum_{[u\;v\;w]}\frac{\partial\left(u_i f\right)}{\partial x_i} \tag{3}$$

The finite volume approximations utilized to convert the partial differential equations for momentum, continuity, and scalar transport into finite volume equations, are listed in Table 1 below.

Most of the listed upwind and central difference algorithms have been used before in a similar manner in the 3D Simulation for Marine and Atmospheric Reactive Transport (3D SMART) (Lawen et al., 2013, 2014) for other transport quantities, such as height h (m), temperature T (°C), salinity S (PSU), and concentration c ($\mathrm{kg\,m^{-3}}$), and on triangle meshes instead of Voronoi meshes.

Table 1. Term Approximation

Term	Convective Upwind	Conservative Central Difference	Central Difference	Diffusive Central Difference	Total Derivative
Advect $u, v, w, h\rho, T, S, c$	∇				
Advect q		∇			
Hydrostatic Pressure			$\frac{\partial}{\partial x_i}$		$\frac{\partial}{\partial x_i}$
Viscous Diffusion				∇^2	
Eddy Shear Rates			$\frac{\partial}{\partial x_i}$		$\frac{\partial}{\partial x_i}$
∇ in Eddy Viscosity's $\nabla \cdot \tau$			$\frac{\partial}{\partial x_i}$		$\frac{\partial}{\partial x_i}$
Smagorinsky Model			$\frac{\partial}{\partial x_i}$		$\frac{\partial}{\partial x_i}$

These approximations of derivatives are expressed in Table 2 in areas A ($\mathrm{m^2}$) and edges e (m) beside an evaluation of derivatives based on the total differential. $\mathbb{1}_{>0}(q)$ denotes the indicator function that evaluates whether the volume flow q_i ($\mathrm{m^3\,s^{-1}}$) through face i into the finite volume fulfills a particular logical condition, such as whether it is bigger than zero, whether the flow is entering or exiting, to facilitate upwinding. $n_i(f)$ denotes here a quantity value at the centroid of a face shared with neighbor i in the neighbor list.

Added to the Wavedyne, the new Voronoi mesh-borne version of the 3D SMART, has been a computation of the derivative based on the total derivative: A polygon's centroid and the centroids of two neighboring cells β and γ constitute a triangle. That is, the total derivative is denoted for one of two edges of a triangle, formed between the centroid of a particular cell and the centroids of two adjacent cells, β and γ, if β is likewise adjacent to γ

$$\delta f_1 = \frac{\partial f_1}{\partial x}\delta x_1 + \frac{\partial f_1}{\partial y}\delta y_1 \tag{4}$$

with particular edge components δx_i, δy_i, and δf_i for edge i but a common $\partial f/\partial x$ and $\partial f/\partial y$ throughout the triangle, yielding

$$\frac{\partial f}{\partial x} = \left(\delta f_1 - \frac{\partial f}{\partial y}\delta y_1\right)/\delta x_1 \tag{5}$$

Likewise the total derivative can be denoted for another edge and the gradient from the left-hand side (LHS) of Equation 2 inserted

$$\delta f_2 = \left(\delta f_1 - \frac{\partial f}{\partial y}\delta y_1\right)\frac{\delta x_2}{\delta x_1} + \frac{\partial f}{\partial y}\delta y_2 \tag{6}$$

which may be resolved for the complementary gradient

$$\frac{\partial f}{\partial y} = \frac{\delta f_2 - \delta f_1 \delta x_2/\delta x_1}{\delta y_2 - \delta y_1 \delta x_2/\delta x_1} \tag{7}$$

Assembling the gradient for asymmetrical Voronoi cells out of triangles requires, furthermore, weighting factors. In Table 2 binary α takes a logical functionality, carrying the value 0 or 1, and is calculated before the simulation to select edge 1 and 2 such that divisions by small numbers are avoided, enhancing accuracy. Likewise, whereas the total derivative's $\partial f/\partial y$ in Table 2 is calculated before $\partial f/\partial x$, the calculation is also conducted in inverted order to provide a substitute in case of a division by zero.

Table 2. Finite Volume Approximations

	Integrated Quantity Flux Approximation
$f'\Big\vert^{\text{convective}}_{\text{upwind}}$	$A^{-1}\sum_i \left[q_i \left(n_i(f)\mathbb{1}_{>0}(q_i) + f_i \mathbb{1}_{\leq 0}(q_i)\right)\right]$
$f'\Big\vert^{\text{conservative}}_{\text{central}}$	$(2A)^{-1}\sum_i \left[q_i f_i + n_i(q) n_i(f)\right]$
$f'\Big\vert_{\text{central}}$	$(2A)^{-1}\sum_i \left[proj_{\perp r}(\boldsymbol{e}_i)\left(n_i(f) - f\right)\right]$
$f''\Big\vert_{\text{central}}$	$A^{-1}\sum_i \left[\lvert\boldsymbol{e}_i\rvert \left(n_i(f) - f\right)\right]$
$f_y\Big\vert_{\substack{\text{total}\\\text{derivative}}}$	$\frac{\alpha\left(f_\beta - f\right) + 0^\alpha\left(f_\gamma - f\right) - \left(\alpha\left(f_\gamma - f\right) + 0^\alpha\left(f_\beta - f\right)\right)\delta x_2/\delta x_1}{\delta y_2 - \delta y_1 \delta x_2/\delta x_1}$
$f_x\Big\vert_{\substack{\text{total}\\\text{derivative}}}$	$\left(\alpha\left(f_\gamma - f\right) - 0^\alpha\left(f_\beta - f\right) - \delta y_1 \partial f/\partial y\right)/\delta x_1$

Arrays for α, β and γ are computed once and for all before the simulation as these arrays depend only on the mesh geometries. Nevertheless, the computational costs of the procedure cannot be assessed as negligible, leading to a doubling of run time vis-á-vis the central difference approximation listed in Table 1 and 2. Algorithm validation has been conducted with a method of manufactured solutions (MMS), which has been submitted separately for publication (Lawen, 2024). The MMS was realized by oscillating the seabed to match the flow field to an analytical solution.

2.1 Continuity

The continuity PDE is obtained by denoting the transport PDE 2 for mass. The conservative form is converted into the convective form by applying the product rule for derivatives in the equation for mass continuity.

$$\frac{\partial m}{\partial t} = -\sum_n \frac{\partial \dot{m}}{\partial x_i} dx_i \tag{8}$$

With $\partial m = \partial\left(\rho V\right)$ ($\mathrm{kg\,m^{-3}\ m^3}$) this is rendered to

$$\frac{\partial\left(\rho V\right)}{\partial t} = -\sum_n \frac{\partial\left(u_i \rho V\right)}{\partial x_i} \tag{9}$$

dividing $V = ph$ by the polygon area p and in a convective form, that is, after application of the product rule

$$\frac{\partial\left(\rho h\right)}{\partial t} = -\sum_n u_i \frac{\partial\left(\rho h\right)}{\partial x_i} - \rho h \sum_n \frac{\partial u_i}{\partial x_i} \tag{10}$$

In the RHS of the approximation below, the first term exhibits the convective form for the quantity h and the second term exhibits the conservative form for a constant quantity $= 1$. Two corresponding finite volume approximations, for the convective and conservative case respectively, can be inserted from Table 2. The first term is approximated with upwinding and the second term with a central difference approximation.

$^{+\delta t}$ denotes a quantity at the subsequent time level. Past Delaunay versions of the 3D SMART's species transport (Lawen et al., 2013, 2014) offered for scalar quantities also semi-implicit matrix reordering algorithms. However, these attained only a tripling of time steps at the expense of FLOPs for the reordering, rendering the net compute gain questionable.

$$\left(h^{+\delta_t}\rho^{+\delta_t} - h\rho\right)\frac{p}{\delta_t} = \overbrace{\sum_m \left[\frac{q_i}{h_i}\left(n(h_i\rho_i)\mathbb{1}_{>0}(q_i) + h_i\rho_i\mathbb{1}_{\leq 0}(q_i)\right)\right]}^{upwind} + \frac{h\rho}{2}\overbrace{\sum_m \left[\frac{q_i}{h_i} + \frac{n(q_i)}{n(h_i)}\right]}^{central\,difference} \tag{11}$$

Here q_i is the volume flow through face i based on the component velocities at the cell's centroid. Meanwhile, $n(q_i)$ is the volume flow based on the component velocities of the neighbor at face i. The latter is included to approximate the volume flow at the face between two cells. The total horizontal flow through cell faces, the summed-up component volume flows, are the products of component velocities and the thereto perpendicular edge components. That is,

$$\frac{q_j}{h_j} = proj_{\perp x}(\boldsymbol{e}_j)u - proj_{\perp y}(\boldsymbol{e}_j)v \tag{12}$$

2.2 Convective material derivative and hydrostatic pressure

The material derivative contains besides the time derivative also advective momentum transport, in the Euler momentum, Cauchy, Navier-Stokes, shallow water, and primitive equations alike. Inserting momentum into the PDE for quantity advection yields

$$\frac{\partial\left(\boldsymbol{u}\rho V\right)}{\partial t} = -\sum_n \frac{\partial\left(u_i\rho\boldsymbol{u}V\right)}{\partial x_i} \tag{13}$$

Applying the product rule to the LHS and RHS yields

$$\boldsymbol{u}\frac{\partial\left(\rho V\right)}{\partial t} + \rho V\frac{\partial\boldsymbol{u}}{\partial t} = -\sum_n \left[u_i\rho V\frac{\partial\boldsymbol{u}}{\partial x_i} + \boldsymbol{u}\frac{\partial\left(u_i\rho V\right)}{\partial x_i}\right] \tag{14}$$

Inserting the conservative form of the continuity PDE into the LHS yields the opportunity to eliminate terms, returning for the LHS and RHS only one term each

$$\rho V\frac{\partial\boldsymbol{u}}{\partial t} = -\rho V\sum_n \left[u_i\frac{\partial\boldsymbol{u}}{\partial x_i}\right] \tag{15}$$

The fluid from equation 13 can be denoted with the velocity in its spatially differential form

$$\partial(\rho\,\boldsymbol{u}\,V)/\partial t = -\sum_n \frac{\partial\left(\rho_i\,\boldsymbol{u}\,V\right)}{\partial x}\frac{dx_i}{dt} \tag{16}$$

which matches the form of the RHS of the total derivative $df = \sum \partial f / \partial s \, ds$ with $ds = [dx_1 ... \, dx_n, \, dt]$ divided by the time increment. Hence,

$$\frac{d(\rho \boldsymbol{u} V)}{dt} = \frac{\partial(\rho \, \boldsymbol{u} \, V)}{\partial t} + \sum_n \frac{\partial(\rho_i \, \boldsymbol{u} \, V)}{\partial x} \frac{dx_i}{dt} \tag{17}$$

or, in consideration of $u_i = dx_i/dt$

$$\frac{d(\rho \boldsymbol{u} V)}{dt} = \frac{\partial(\rho \, \boldsymbol{u} \, V)}{\partial t} + \sum_n \frac{\partial(u_i \, \boldsymbol{u} \, \rho_i \, V)}{\partial x} \tag{18}$$

PDE and FVE can, hence, be configured as Euler equation by including forces. As per Newton's second law holds for force $\boldsymbol{F}$ and momentum $m\boldsymbol{u}$

$$\boldsymbol{F} = d(m\boldsymbol{u})/dt \tag{19}$$

Given $m\boldsymbol{u} = \rho \, V \, \boldsymbol{u}$, the net force in the LHS is obtained by summing up all forces F_j in a free body diagram.

$$\sum \boldsymbol{F}_j = \sum \frac{\partial(u_i m \boldsymbol{u})}{\partial x_i} + \frac{\partial m \boldsymbol{u}}{\partial t} \tag{20}$$

In terms of FVE approximation, a quantity balance for a regular or irregularly shaped finite volume returns for quantity f, transported with upwind approximation in volume flows q_i into volume V,

$$\frac{\partial(fV)}{\partial t} = \sum_m (q_i \, (n(f_i) \mathbb{1}_{>0}(q_i) + f_i \mathbb{1}_{\leq 0}(q_i))) \tag{21}$$

$\mathbb{1}$ is the indicator function that denotes the logical condition of using quantity values of neighboring cells for faces i where volume flows q_i are positive, i.e. in-flowing. The component velocity basis for the volume flows determines whether this FVE corresponds to the conservative or convective case. The latter is the case if the centroid's component velocities is applied to all faces. Inserting momentum into the FVE 21 for quantity advection yields

$$\frac{\partial(\boldsymbol{u} \rho V)}{\partial t} = \sum_i (q_i \, (\rho n(\boldsymbol{u}_i) \mathbb{1}_{>0}(q_i) + \rho \boldsymbol{u}_i \mathbb{1}_{\leq 0}(q_i))) \tag{22}$$

If the force acting on surfaces i of the irregular fluid parcel is pressure, then as per $F_i = (\delta_P)_i proj_{\perp r}(\boldsymbol{A}_i)$, with the pressure difference δ_P and the vector of orthogonal component areas $proj_{\perp r}(\boldsymbol{A}_i)$, holds

$$\sum_i ((\delta_P)_i proj_{\perp r}(\boldsymbol{A}_i)) = \sum \frac{\partial(u_i \boldsymbol{p})}{\partial x_i} + \frac{\partial \boldsymbol{p}}{\partial t} \tag{23}$$

Due to a difference in surface height $\delta_h/2$ between adjacent centroids and the edge of the considered cell, follows

$$g \sum_i \left[\left(\rho \frac{\delta_h}{2} \right)_i proj_{\perp r}(\boldsymbol{A}_i) \right] = \sum \frac{\partial(u_i m \boldsymbol{u})}{\partial x_i} + \frac{\partial m \boldsymbol{u}}{\partial t} \tag{24}$$

$$g \sum_i \left[\left(\rho \frac{\delta_h}{2} \right)_i proj_{\perp r}(\boldsymbol{A}_i) \right] = \sum \frac{\partial(u_i \rho V \boldsymbol{u})}{\partial x_i} + \frac{\partial(\rho V \boldsymbol{u})}{\partial t} \tag{25}$$

which is again inserted in the RHS of the FVE.

$$g\sum_i \left[\left(\rho\frac{\delta_h}{2}\right)_i proj_{\perp r}(\boldsymbol{A}_i)\right] = \sum_i \left(q_i\left(\rho n(\boldsymbol{u}_i)\mathbb{1}_{>0}(q_i) + \rho\boldsymbol{u}_i\mathbb{1}_{\leq 0}(q_i)\right)\right) + \frac{\partial(\rho V\boldsymbol{u})}{\partial t} \tag{26}$$

With a discrete time derivative and the term for Coriolis acceleration this yields

$$\frac{\rho V\left(\boldsymbol{u}^{+\delta t} - \boldsymbol{u}\right)}{\delta t} = g\sum_i \left[\left(\rho\frac{\delta_h}{2}\right)_i proj_{\perp r}(\boldsymbol{A}_i)\right] - \sum_i \left(q_i\left(\rho n(\boldsymbol{u}_i)\mathbb{1}_{>0}(q_i) + \rho\boldsymbol{u}_i\mathbb{1}_{\leq 0}(q_i)\right)\right) + F_c \tag{27}$$

The method is first order in space and time to attain high resolution meshes (Figure 6) to resolve waves while remaining efficient in terms of FLOPs: to resolve waves, the cell size should be a log order below the part of the wave spectrum of interest, i.e. maximizing cell count and minimizing FLOPs per cell.

2.3 Coriolis acceleration

Forces, including rotational pseudo-forces, can be substituted into the left-hand side (LHS) of Equation 20. For the latter, the LHS has to be transformed into the earth's rotating latitude-longitude reference frame. To observe the acceleration in a rotating reference frame, it can be denoted in terms of the spatial vector relative to the inertial reference frame:

$$\frac{d^2\boldsymbol{r}}{dt}_i = \left[\frac{d}{dt} + \boldsymbol{\Omega}\times\right]\left[\frac{d\boldsymbol{r}}{dt} + \boldsymbol{\Omega}\times\boldsymbol{r}\right] \tag{28}$$

where i indicates the inertial reference frame. This yields for all n components denoted in momentum vector $m\boldsymbol{u}$:

$$\boldsymbol{F} - m\frac{d\boldsymbol{\omega}}{dt}\times\boldsymbol{r} - 2m\left(\boldsymbol{\omega}\times\boldsymbol{v}\right) - m\boldsymbol{\omega}\times\left(\boldsymbol{\omega}\times\boldsymbol{r}\right) = \frac{\partial m\boldsymbol{u}}{\partial t} + \sum_{\boldsymbol{r}=[x_1\ldots x_n]}\left(u_i\frac{\partial m\boldsymbol{u}}{\partial x_i}\right) \tag{29}$$

with $\boldsymbol{\Omega}$ being earth's angular velocity. This procedure recovers a term to account for earth's rotation alone. The effects due to Earth's axial tilt, which is accounted for in the insolation simulation for surface heat exchange, inclination relative to the solar plane, and the Sun's inclination relative to the galactic plane, are unanimously deemed negligible at the scale of the required transport accuracy and given other uncertainties, such as due to bathymetric uncertainty. Likewise earth's angular velocity is considered as constant and, hence, its time derivative vanishes:

$$\boldsymbol{F} - 2m\left(\boldsymbol{\omega}\times\boldsymbol{v}\right) - m\boldsymbol{\omega}\times\left(\boldsymbol{\omega}\times\boldsymbol{r}\right) = \frac{\partial m\boldsymbol{u}}{\partial t} + \sum_{\boldsymbol{r}=[x_1\ldots x_n]}\left(u_i\frac{\partial m\boldsymbol{u}}{\partial x_i}\right) \tag{30}$$

The vertical component of the Coriolis acceleration is deemed negligible (Kundu et al., 2016) and heavily masked by imperfectly defined vertical turbulent momentum transport. Evaluating the cross products yields for earth's zonal and meridional dimensions a negligible term with quadratic angular velocity, a perpendicular centripetal, radially inward acceleration, absent which

$$F_x + 2\,m\,\omega\sin(\phi)v = \frac{\partial mu}{\partial t} + \sum\left(u_i\frac{\partial mu}{\partial x_i}\right) \tag{31}$$

$$F_y - 2\,m\,\omega\sin(\phi)u = \frac{\partial mv}{\partial t} + \sum\left(u_i\frac{\partial mv}{\partial x_i}\right) \tag{32}$$

is obtained for a particular latitude ϕ (rad) where earth's angular velocity ω ($\mathrm{rad\,s^{-1}}$) is given with $2\pi(24 \times 60^2\mathrm{s})^{-1}$. As the Coriolis term does not contain any derivative, no approximation is required.

2.4 Viscous stress, turbulence, LES, and RANS

The consideration of surface forces also accounts for the internal friction of the fluid, the viscosity. Each of the three component velocities, at the centroids of the faces of the examined control volume, undergoes strain in three spatial dimensions, yielding nine strain rate elements which are commonly presented in tensor form as shown in equation 1. Note, tensor calculus falls here into the confines of matrix calculus. The viscous stress tensor is usually denoted in the form below including the Nabla operator from the first-order Taylor expansion, to attain the differential notation of the force balance at the infinitesimal control volume. For example, for the first component velocity, the dot product yields for the first tensor row $\partial\tau_{xx}/\partial x + \partial\tau_{xy}/\partial y + \partial\tau_{xz}/\partial z$.

The Navier-Stokes PDE is set apart from the Cauchy momentum PDE by being specified for Newtonian fluids where – assuming incompressibility – stress τ_{ij} is linearly proportional to the sum of the gradient of velocity i in direction j and the gradient of velocity j in direction i. The proportionality coefficient μ_{ij} is termed the viscosity. The entirety of all stresses, denoted in the stress tensor, can, hence, be substituted by the proportionality of incompressible Newtonian fluids to the sum of the strain rate tensor and its transpose. Note, the absence of volume viscosity is warranted due to the assumption of incompressibility.

$$\boldsymbol{\nabla} \cdot \begin{pmatrix} \tau_{xx} & \tau_{xy} & \tau_{xz} \\ \tau_{yx} & \tau_{yy} & \tau_{yz} \\ \tau_{zx} & \tau_{zy} & \tau_{zz} \end{pmatrix} = \boldsymbol{\nabla} \cdot \left(\begin{pmatrix} \mu_{xx}\frac{\partial u}{\partial x} & \mu_{xy}\frac{\partial u}{\partial y} & \mu_{xz}\frac{\partial u}{\partial z} \\ \mu_{yx}\frac{\partial v}{\partial x} & \mu_{yy}\frac{\partial v}{\partial y} & \mu_{yz}\frac{\partial v}{\partial z} \\ \mu_{zx}\frac{\partial w}{\partial x} & \mu_{zy}\frac{\partial w}{\partial y} & \mu_{zz}\frac{\partial w}{\partial z} \end{pmatrix} + \begin{pmatrix} \mu_{xx}\frac{\partial u}{\partial x} & \mu_{yx}\frac{\partial v}{\partial x} & \mu_{zx}\frac{\partial w}{\partial x} \\ \mu_{xy}\frac{\partial u}{\partial y} & \mu_{yy}\frac{\partial v}{\partial y} & \mu_{zy}\frac{\partial w}{\partial y} \\ \mu_{xz}\frac{\partial u}{\partial z} & \mu_{yz}\frac{\partial v}{\partial z} & \mu_{zz}\frac{\partial w}{\partial z} \end{pmatrix} \right) \tag{33}$$

The RHS contains the strain rate tensor and its transpose. In the case of molecular viscosity, that is, momentum transport due to molecular diffusion and interaction, an isotropic and spatially constant coefficient is assumed for all nine ij combinations. As per the latter assumption, the viscosity coefficient can be denoted outside the tensor.

$$\boldsymbol{\nabla} \cdot \mu \left(\begin{pmatrix} \frac{\partial u}{\partial x} & \frac{\partial u}{\partial y} & \frac{\partial u}{\partial z} \\ \frac{\partial v}{\partial x} & \frac{\partial v}{\partial y} & \frac{\partial v}{\partial z} \\ \frac{\partial w}{\partial x} & \frac{\partial w}{\partial y} & \frac{\partial w}{\partial z} \end{pmatrix} + \begin{pmatrix} \frac{\partial u}{\partial x} & \frac{\partial v}{\partial x} & \frac{\partial w}{\partial x} \\ \frac{\partial u}{\partial y} & \frac{\partial v}{\partial y} & \frac{\partial w}{\partial y} \\ \frac{\partial u}{\partial z} & \frac{\partial v}{\partial z} & \frac{\partial w}{\partial z} \end{pmatrix} \right) \tag{34}$$

Inserting term 34 in equation 33 and resolving its dot product yields for the first row, that is, for the viscous stress term of component velocity u

$$\frac{\partial \tau_{xx}}{\partial x} + \frac{\partial \tau_{xy}}{\partial y} + \frac{\partial \tau_{xz}}{\partial z} = \mu \left(\frac{\partial \left(\frac{\partial u}{\partial x} + \frac{\partial u}{\partial x} \right)}{\partial x} + \frac{\partial \left(\frac{\partial u}{\partial y} + \frac{\partial v}{\partial x} \right)}{\partial y} + \frac{\partial \left(\frac{\partial u}{\partial z} + \frac{\partial w}{\partial x} \right)}{\partial z} \right) \tag{35}$$

In Eulerian fluid dynamics, that is, continuum mechanics, the assumption of continuous variables flows directly from the very concept under consideration and is presumed for the quantities' derivatives as well. Therefore, Clairaut's theorem can be applied, rendering the order of partial differentiation immaterial. This assumption breaks down at quantity jumps. Yet at infinite gradients, Eulerian diffusive models break down anyway. Fortunately, such conditions are, at the considered scale, not

present in the described coastal ocean systems. Therefore, partial derivatives in the LHS can be sorted as follows

$$\frac{\partial \tau_{xx}}{\partial x} + \frac{\partial \tau_{xy}}{\partial y} + \frac{\partial \tau_{xz}}{\partial z} \mu \left(\frac{\partial^2 u}{\partial x^2} + \frac{\partial^2 u}{\partial y^2} + \frac{\partial^2 u}{\partial z^2} \right) + \mu \frac{\partial \overbrace{\left(\frac{\partial u}{\partial x} + \frac{\partial v}{\partial y} + \frac{\partial w}{\partial z} \right)}^{=0}}{\partial x} \tag{36}$$

Here the insertion of the continuity PDE $\nabla \boldsymbol{u} = 0$ eliminates three of the partial derivatives, yielding for the entire system of PDEs

$$\frac{\partial(\rho\, \boldsymbol{u}\, V)}{\partial t} + \sum_n \frac{\partial \left(u_i \rho_i\, \boldsymbol{u}\, V\right)}{\partial x} = \boldsymbol{F} + \mu \left(\frac{\partial^2 \boldsymbol{u}}{\partial x^2} + \frac{\partial^2 \boldsymbol{u}}{\partial y^2} + \frac{\partial^2 \boldsymbol{u}}{\partial z^2} \right) \tag{37}$$

Molecular viscosity is isotropic and largely constant and can, therefore, due to being constant, be denoted outside the derivative. Yet, eddy viscosity is not at all constant. In the case of eddy viscosity, the Smagorinsky model assumes horizontally isotropic viscosity. Furthermore,

$$\frac{\partial w}{\partial x} \ll \frac{\partial u}{\partial x}, \quad \frac{\partial w}{\partial x} \ll \frac{\partial u}{\partial y}, \quad \frac{\partial w}{\partial x} \ll \frac{\partial v}{\partial x} \tag{38}$$

and the analogous for $\partial w / \partial y$, yielding

$$\boldsymbol{\nabla} \cdot \left(\begin{pmatrix} k\frac{\partial u}{\partial x} & k\frac{\partial u}{\partial y} & k_z\frac{\partial u}{\partial z} \\ k\frac{\partial v}{\partial x} & k\frac{\partial v}{\partial y} & k_z\frac{\partial v}{\partial z} \\ k\frac{\partial w}{\partial x} & k\frac{\partial w}{\partial y} & k_z\frac{\partial w}{\partial z} \end{pmatrix} + \begin{pmatrix} k\frac{\partial u}{\partial x} & k\frac{\partial v}{\partial x} & 0\frac{\partial w}{\partial x} \\ k\frac{\partial u}{\partial y} & k\frac{\partial v}{\partial y} & 0\frac{\partial w}{\partial y} \\ k_z\frac{\partial u}{\partial z} & k_z\frac{\partial v}{\partial z} & k_z\frac{\partial w}{\partial z} \end{pmatrix} \right) \tag{39}$$

with horizontally isotropic eddy viscosity k and vertical eddy viscosity k_z. Therefore, Clairaut's theorem cannot be applied except for the third row of the transpose. That is, the transpose of the strain rate tensor remains relevant. The partial derivatives are, thus, collected differently, yielding for the horizontal component velocities

$$\frac{\partial(\rho\, u\, V)}{\partial t} + \sum_n \frac{\partial \left(u_i \rho_i\, u\, V\right)}{\partial x} = \boldsymbol{F} + 2\frac{\partial \left(k \partial u / \partial x\right)}{\partial x} + \frac{\partial \left(k \left(\partial u / \partial y + \partial v / \partial x\right)\right)}{\partial y} + \frac{\partial \left(k_z \partial u / \partial z\right)}{\partial z} \tag{40}$$

$$\frac{\partial(\rho\, v\, V)}{\partial t} + \sum_n \frac{\partial \left(u_i \rho_i\, v\, V\right)}{\partial x} = \boldsymbol{F} + 2\frac{\partial \left(k \partial v / \partial y\right)}{\partial y} + \frac{\partial \left(k \left(\partial v / \partial x + \partial u / \partial y\right)\right)}{\partial x} + \frac{\partial \left(k_z \partial v / \partial z\right)}{\partial z} \tag{41}$$

The dot product of the transpose of the strain rate tensor for the third row, the vertical component velocity w:

$$\boldsymbol{\nabla} \cdot \left(k\frac{\partial w}{\partial x} + k\frac{\partial w}{\partial y} + k_z\frac{\partial w}{\partial z} \right) + \frac{\partial \left(k_z \frac{\partial u}{\partial z}\right)}{\partial x} + \frac{\partial \left(k_z \frac{\partial v}{\partial z}\right)}{\partial y} + \frac{\partial \left(k_z \frac{\partial w}{\partial z}\right)}{\partial z} \tag{42}$$

Applying the product rule and sorting terms produces

$$\boldsymbol{\nabla} \cdot \left(k\frac{\partial w}{\partial x} + k\frac{\partial w}{\partial y} + k_z\frac{\partial w}{\partial z} \right) + \frac{\partial k_z}{\partial x}\frac{\partial u}{\partial z} + \frac{\partial k_z}{\partial y}\frac{\partial v}{\partial z} + \frac{\partial k_z}{\partial z}\frac{\partial w}{\partial z} + k_z \left(\frac{\partial \frac{\partial u}{\partial z}}{\partial x} + \frac{\partial \frac{\partial v}{\partial z}}{\partial y} + \frac{\partial \frac{\partial w}{\partial z}}{\partial z} \right) \tag{43}$$

For the last three terms, Clairaut's theorem can again be applied, changing the order of partial differentiation. Furthermore, some terms are approximated with finite differences.

$$\boldsymbol{\nabla} \cdot \left(k\frac{\partial w}{\partial x} + k\frac{\partial w}{\partial y} + k_z\frac{\partial w}{\partial z} \right) + \frac{\delta k_z}{\delta x}\frac{\delta u}{\delta z} + \frac{\delta k_z}{\delta y}\frac{\delta v}{\delta z} + \frac{\delta k_z}{\delta z}\frac{\delta w}{\delta z} + k_z\frac{\partial \overbrace{\left(\frac{\partial u}{\partial x} + \frac{\partial v}{\partial y} + \frac{\partial w}{\partial z} \right)}^{=0}}{\partial z} \tag{44}$$

yielding again the opportunity to exploit the continuity PDE to eliminate terms. Also, the finite difference approximation yields the opportunity to rearrange divisors

$$\boldsymbol{\nabla} \cdot \left(k\frac{\partial w}{\partial x} + k\frac{\partial w}{\partial y} + k_z\frac{\partial w}{\partial z} \right) + \frac{\delta k_z}{\delta z}\overbrace{\left(\frac{\delta u}{\delta x} + \frac{\delta v}{\delta y} + \frac{\delta w}{\delta z} \right)}^{\approx 0} \tag{45}$$

recovering the finite difference approximation of the continuity PDE, which is approximately zero, and, thus, eliminating further terms. Inserted into the PDE for the vertical component velocity this yields

$$\frac{\partial(\rho\, w\, V)}{\partial t} + \sum_n \frac{\partial\left(u_i \rho_i\, w\, V\right)}{\partial x} = \boldsymbol{F} + \frac{\partial\left(k\partial w/\partial x\right)}{\partial x} + \frac{\partial\left(k\partial w/\partial y\right)}{\partial y} + \frac{\partial\left(k_z\partial w/\partial z\right)}{\partial z} \tag{46}$$

Table 1 and 2 list the selectable approximations for the eddy diffusive terms. Transport unresolved by the mesh is at the smallest scale molecular diffusion that is present also during laminar flow. Negligible molecular diffusion but also unresolved eddies are usually modeled as random, that is, diffusive phenomena and referred to by the fictitious quantity eddy diffusion.

Direct numerical simulation (DNS) is computationally prohibitively expensive for geophysical scales absent a quantum computing resource (Itani, 2021; Bharadwaj and Sreenivasan, 2022). Henceforth, unresolved turbulence is treated with two baroque chains of fictitious models and quantities: 1.) Reynolds-averaged Navier Stokes (RANS) and 2.) large eddy simulations (LES). In the first approach, transient fluctuations are split off the modeled velocity, whereas, in the second, transport is filtered by deducting (Smagorinsky, 1963) spatially unresolved transport. That is, the former smooths over time, the latter smooths over space, and both can be used in the same model for the vertical and horizontal respectively (Yu et al., 2017, 2018).

The RANS approach is more receptive to account for buoyancy which is important for vertical turbulence whereas LES, developed by Smagorinsky, is computationally more effective for isotropic flows which are a valid description of the horizontal. Therefore, RANS models, in particular k-ϵ models, are commonly used for the vertical and an LES-Smagorinsky model for the horizontal. The same approach has been selected for this model and documented in subsequent sections.

The transport PDEs derived above, including a diffusive term for turbulence and in conjunction with a density quantifying PDE is termed the primitive equations where primitive corresponds to its basic governing utility and not a lack in sophistry. Or, if inertial considerations are restricted to two dimensions and the vertical is approximated with mere continuity, then the yielded set of PDE is termed shallow water equations.

2.5 Smagorinsky turbulence

Transport of vector and scalar quantities is deemed split into a resolved and an unresolved component. This step is commonly referred to as filtering with a filtered velocity $\bar{u}$ and an unresolved residual velocity. Underlying the Smagorinsky model is the

assumption that Reynolds stress can be modeled with the rate of strain tensor, introducing another fictitious viscosity that is itself modeled by the rate of strain tensor. The Smagorinsky model has inherent the assumption of an even weighting of the fluctuating velocity. The averaging in the filter function can also introduce a heavier weight close to the centroids given that the velocities are stored at the centroid.

The Smagorinsky model corresponds only to a uniform isotropic filter, also termed box filter. Gaussian bell-shaped filter functions exist as well that particularly sample the fluctuation velocity at the centroids while still smoothing fluctuations. The eddy viscosity is dependent on the filter size, here the Voronoi cell size. Molecular viscosity is usually ignored, given that it is logarithmic orders of magnitude smaller than eddy viscosity. The Smagorinsky model is simpler than the RANS model by assuming an isotropic turbulence, which is warranted in the horizontal plane but not for the vertical plane.

In the Smagorinsky model, the strain rate tensor of the resolved flow represents the local deformation of the flow. The model is obtained from Kolmorov modeling (Kolmogorov, 1941) of the turbulent energy dissipation from the average of the fluctuating velocity where a proportionality of the former to the Reynolds stress is inferred from dimensional analysis. The utilization of a diffusive term under the assumption of random and, thus, gradient driven transport, is readily obtained from the fluid's Lagrangian description given that random transport holds in the thermodynamic Lagrangian domain at every scale of unresolved geometry.

$$k_H = \frac{C_S P}{2} \sqrt{\left(\frac{\partial u}{\partial x}\right)^2 + \left(\frac{\partial v}{\partial y}\right)^2 + 2^{-1}\left(\frac{\partial v}{\partial x} + \frac{\partial u}{\partial y}\right)^2} \tag{47}$$

with the Smagorinsky coefficient C_S. The eddy diffusivity constant is usually (Yang and Khangaonkar, 2008; Chen et al., 2011) horizontally treated as isotropic but computed separately for the vertical. The eddy diffusivity is for momentum transport modeled with the eddy viscosity μ, which can be set for the horizontal or vertical as prognostic or diagnostic. That is, in the latter case, a value obtained from a parameter identification is applied. Otherwise, in the prognostic case, the horizontal eddy viscosity is computed with the Smagorinsky model.

Numerical diffusion is to be expected as well, that is, artificial diffusion inherent to continuum descriptions of physics. Numerical diffusion does not pose a detriment to the stability but to the accuracy of a simulation by inflating eddy diffusion. Nevertheless, LES and RANS models permit nominal compliance with the Navier-Stokes PDE, comprehensiveness in approximating all terms, or may entail stability benefits that a diffusive term conveys to some algorithms.

The Smagorinsky model has been defined as an L2-norm of derivatives of the component velocities. The evaluation of the Cartesian gradient at the centroids is not readily available in unstructured meshes and requires dedicated computation (Skamarock et al., 2012). Given that magnitudes of other uncertainties are of higher logarithmic orders in LES and RANS models, it appears questionable to expend FLOPs to refine the computation of the derivatives in Eq. 47 to compute estimates for this fictitious quantity. Nevertheless, to not have to quantify the uncertainty due to these interpolations, the derivatives of the velocity components at the centroid are here rigorously computed by applying the total derivative to each triangle spanned between a centroid and two adjacent neighbors. Most of these computations can be calculated ahead of the simulation and stored in auxiliary arrays as provided in Table 2.

The filtered transport in the eddy diffusive terms requires a proportionality coefficient to link the strain rate to an eddy diffusive

force. In coastal ocean momentum transport, it is commonly assumed that this coefficient grows with the LES spatial filter, represented by the Voronoi polygon size P, and the strain rate terms in the root of Equation 47 above. Algorithms to compute gradients are listed in Table 1 and 2. All geometric meta-quantities are calculated in advance ahead of the simulation and stored to minimize the computational load.

2.6 Hydrodynamic boundary conditions

For vector quantities, that is, velocity components, the hydrostatic pressure gradient ascertains that each finite volume with a no-flux face does not grow out of bounds. The no-flux boundary is simply attained by setting all fluxes through the boundary face to zero. For scalar quantities, that is, quantities absent a hydrostatic pressure term, such as temperature, salinity, sediment, and tracer, the free-slip boundary condition ascertains that quantities do not grow out of bounds. The free-slip boundary condition ascertains that the velocity vector in the finite volume is parallel to the boundary. That is, no component is perpendicular to a solid boundary face. At open boundary conditions that connect the model to the open sea, the surface elevation is set to the surveyed tidal meter time series or tidal data from any other source.

Rigor in depicting bottom stress is limited by a usually unknown roughness distribution of the vast seafloor. Some assumptions have heretofore though been made: Absent a velocity to shed from or fluid to interact with, no friction force can act, rendering plausible the assumption of bottom stress being dependent on velocity and density. If an advected fluid particle encounters and is exerted upon by a roughness element, then the number of encounters is, absent orientation of the roughness element, in such Lagrangian model proportional to the advecting velocity's magnitude and particle density. Furthermore, the net force exerted can, as any force, be denoted in its components, that is, in terms of velocity components as momentum is removed from the same. Therefore, the bottom stress proportionality is obtained and rendered an equation (Feddersen et al., 2003; Faria et al., 1998) by introducing a proportionality coefficient

$$\begin{aligned} \boldsymbol{\tau} &\propto \rho\langle\|\boldsymbol{u}\|\boldsymbol{u}\rangle \\ \boldsymbol{\tau} &= \rho c_d\langle\|\boldsymbol{u}\|\boldsymbol{u}\rangle \end{aligned} \tag{48}$$

with the coefficient c_d being termed drag coefficient. Evident with Equation 48 becomes that, for a particular stress $\boldsymbol{\tau}$, the drag coefficient c_d depends on the height above the bottom given the velocity's dependency on this height. For example, if a slim bottom layer is modeled, utilizing a slow segment within the vertical velocity profile, then the drag coefficient grows.

An estimate for c_d is usually obtained (Grant and Madsen, 1979) by applying the Prandtl-Kármán logarithmic velocity profile to oceanic applications, that is,

$$\|\boldsymbol{u}\| = \frac{u_*}{\kappa}\ln\left(\frac{z}{z_0}\right) \tag{49}$$

where the friction velocity is defined with

$$\|\boldsymbol{\tau}\| = \rho u_*^2 \tag{50}$$

with the bottom stress $\boldsymbol{\tau}$, the friction velocity u_*, the Kármán constant $\kappa = 0.4$, the roughness length z_0, and the height above the seafloor z. Bottom drag has been specified by conducting parameter identifications for the friction velocity and

drag coefficient (Faria et al., 1998), or by identifying a suitable roughness length (Isobe and Beardsley, 2006; Weisberg and Zheng, 2006; Yang and Khangaonkar, 2008). Yet, whereas the drag coefficient depends on the bottom layer height, the friction velocity depends on the local velocity. Both are, thus, not independent of transient quantities. Therefore, for the purpose of modeling various depths and flow regimes, only the roughness length is sufficiently fundamental to hold for the entire tidal cycle. Resolving Equation 49 for u_* and specifying the RHS for two heights, eliminates the friction velocity

$$\frac{\kappa\|\boldsymbol{u_1}\|}{\ln\left(\frac{z_1}{z_0}\right)} = \frac{\kappa\|\boldsymbol{u_2}\|}{\ln\left(\frac{z_2}{z_0}\right)} \tag{51}$$

and, after rearrangements, resolves to the ubiquitous form for roughness length identification in atmospheric and oceanic applications alike:

$$\ln z_0 = \frac{\|\boldsymbol{u_1}\|\ln z_2 - \|\boldsymbol{u_2}\|\ln z_1}{\|\boldsymbol{u_1}\| - \|\boldsymbol{u_2}\|} \tag{52}$$

The drag coefficient c_d in the boundary condition is then obtained by taking the magnitude of the LHS- and RHS-vector in Equation 48 whilst substituting for the LHS the RHS of Equation 50.

$$\rho u_*^2 = \|\rho c_d \langle\|\boldsymbol{u}\|\boldsymbol{u}\rangle\| \tag{53}$$

Furthermore, Equation 49, resolved for the friction velocity, substitutes the same in Equation 53.

$$\left(\frac{\kappa\|\boldsymbol{u}\|}{lnz - lnz_0}\right)^2 = c_d\|\boldsymbol{u}\|\|\boldsymbol{u}\| \tag{54}$$

Thus, yielding the common form (Chen et al., 2011) for calculating the drag coefficient distribution from the roughness length

$$c_d(x,y,t) = \left(\frac{\kappa}{lnz(x,y,t) - lnz_0}\right)^2 \tag{55}$$

Denoted in Equation 55 is explicitly, that $c_d(x,y,t)$ is not a constant but a horizontal distribution, if the layer thickness $z(x,y,t)$ is not constant. Seabed change or tidal transience, depending on the layer configuration, can result in a time dependency.

2.7 Sediment transport, waves, and entrainment

Sediment is transported like any other constituent with the addition of sediment settling and bottom sediment entrainment. A mass balance for the sediment type C returns

$$\frac{\partial C}{\partial t} + \frac{\partial(uC)}{\partial x} + \frac{\partial(vC)}{\partial y} + \frac{\partial\left((w-w_s)C\right)}{\partial z} = \frac{\partial}{\partial x}\left(D_x\frac{\partial C}{\partial x}\right) + \frac{\partial}{\partial y}\left(D_y\frac{\partial C}{\partial y}\right) + \frac{\partial}{\partial z}\left(D_z\frac{\partial C}{\partial z}\right) - E \tag{56}$$

with the entrainment term E. The consideration for eddy diffusion in the chapters above have shown that the horizontal eddy diffusive coefficients are horizontally isotropic. Furthermore, the insertion of continuity permits to denote the velocities outside of the derivatives.

$$\frac{\partial C}{\partial t} + u\frac{\partial C}{\partial x} + v\frac{\partial C}{\partial y} + (w-w_s)\frac{\partial C}{\partial z} = \frac{\partial}{\partial x}\left(A_h\frac{\partial C}{\partial x}\right) + \frac{\partial}{\partial y}\left(A_h\frac{\partial C}{\partial y}\right) + \frac{\partial}{\partial z}\left(D_z\frac{\partial C}{\partial z}\right) - E \tag{57}$$

The settling velocity w_s for fine sediment, set in the input file, can be calculated with Stoke's law

$$w_s = \frac{d^2 g(\rho_s - \rho)}{18\mu} \tag{58}$$

where d is the diameter of the sediment particle (m), g is the acceleration due to gravity $(\mathrm{m\,s^{-2}})$, ρ_s is the density of the sediment particle $(\mathrm{kg\,m^{-3}})$, ρ is the density of the fluid $(\mathrm{kg\,m^{-3}})$, and μ is the dynamic viscosity of the fluid $(\mathrm{kg\,m^{-1}\,s^{-1}})$. The influence of orbital wave motion on near-bottom tidal currents depends on the length of agitating waves. If conditions are calm with wind waves exhibiting wavelengths much smaller than twice the water depth, then the perturbation of near-bottom tidal currents due to orbital wave motion remains small or insignificant. If conditions are sufficiently agitated, such that wavelengths reach in size to the order of magnitude of the water depth, then wave orbital motion considerably drives bottom currents. Additionally, high energy waves yield disproportionate increases in erosive fluxes, contributing considerably to shoreline development. The Rouse number that indicates whether sediment entrainment or deposition occurs, is given with

$$Ro = \frac{w_s}{\kappa u_*} \tag{59}$$

The survey current meter recorded for sheltered conditions wavelengths not exceeding 0.5 (m). Therefore, erosive fluxes have been simulated for three conditions with a dedicated high resolution mesh for wave-resolving simulations as detailed in Subsection 3.4 of Section 3: tidal currents during sheltered conditions and during two high energy wave scenarios. Waves are approximated as second order Stokes waves as per the Le Méhauté diagram.

3 Application

Documentation to step-by-step build the model is given in below subsections on meshing 3.1 and case dependent horizontal as well as vertical boundary conditions 3.2. That is, setting tidal boundary conditions to drive the model and the bottom friction parameter to attenuate it respectively. The water body modeled is shown in Figure 1. A highly resolved beach model for wave simulations is nested within a model for the entirety of the bay. Five survey locations in Doha Bay provided for boundary forcing (two) and triple validation, besides examining the same for two seasons.

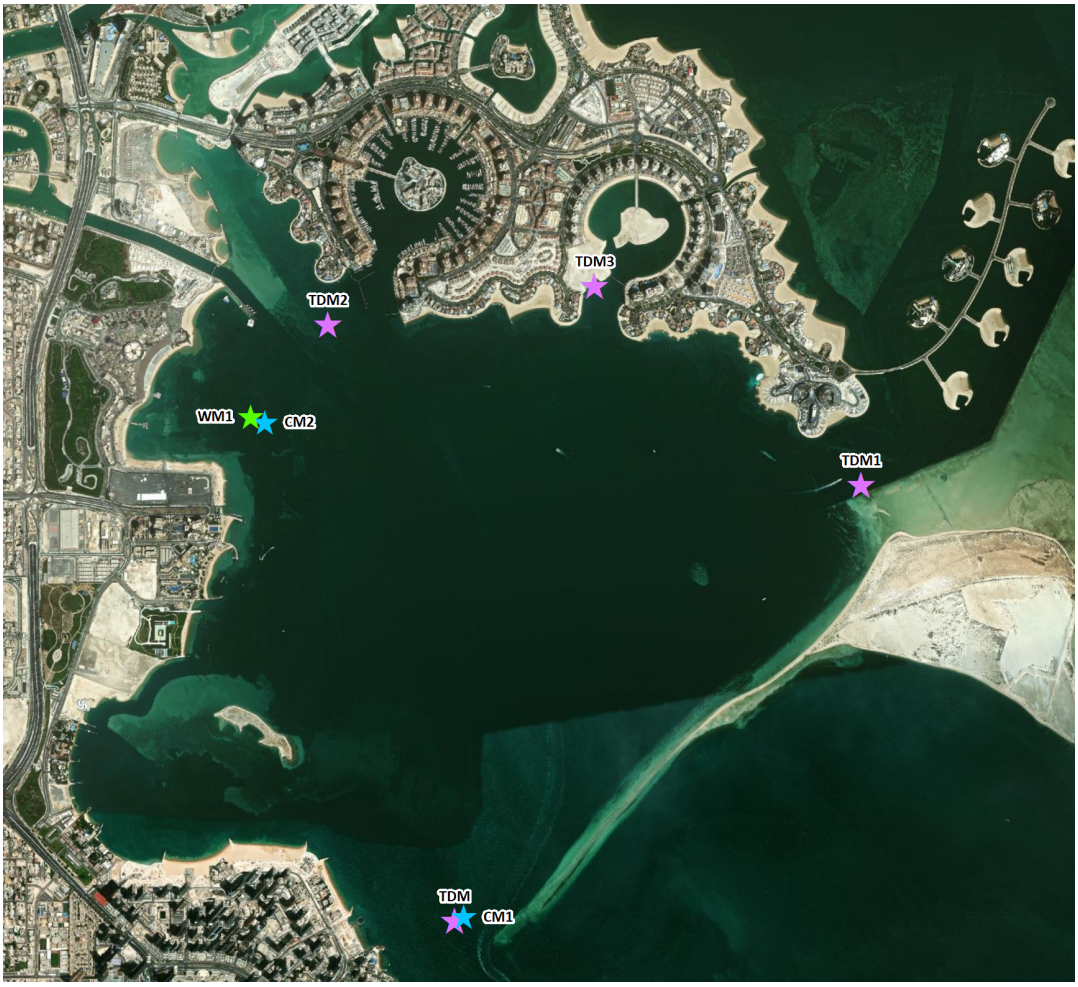

Figure 1. Doha Bay, © Google Earth 2023.

3.1 Meshing

To obtain the horizontal geometry of the sea surface, a satellite image, as exhibited in Figure 1, can be downloaded from Google Earth or any other image, map, or CAD drawing be used. The coastline and boundary are then marked with a 24-bit RGB code identifier in a .bmp file in any .bmp editing tool. All land pixels are then automatically flood-filled after setting all other pixels to 0 with the logical array and flood fill function `excise('image.bmp',RGB)` with a particular 24-bit `RGB` color, that is, with maximal component values `[255 255 255]`.

Maps and CAD designs of future developments can be superimposed with the script `overlay`. The mesh is created directly from the .bmp with the mesh generator `meshing2a('image.bmp')`. The latter automatically provides for a higher resolution at the boundary between land and sea by first distributing Voronoi polygon seeds by sweeping along the shore with

increasing distances followed by three iterations of mesh relaxation. The relaxation algorithm redistributes as per Lloyd's algorithm but is based on a discrete tesselation. The mesh, depicted in Figure 2, is geo-referenced by marking two reference coordinates, (x_a, y_a) and (x_b, y_b) within the 24-bit .bmp file fed to the meshing generator with a particular 24-bit `RGB` color.

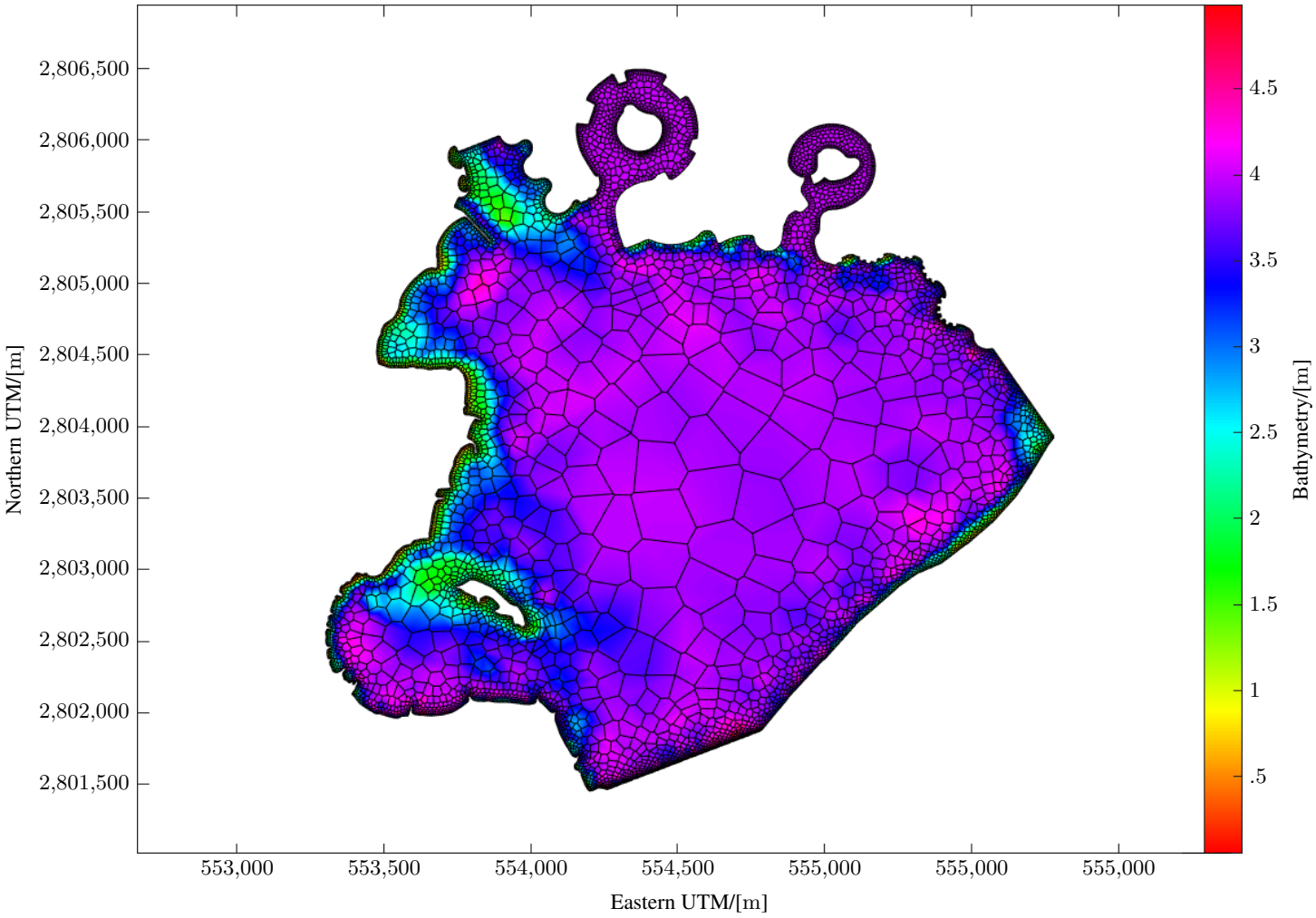

Figure 2. Bathymetry with corrected Marina design depth. The wave-resolving mesh is shown in Figure 6.

The function `[x1,y1,xd,yd] = coord23('.bmp',RGB,xa,ya,xb,yb)` then returns the coordinates of the bottom left corner (`x1,y1`) of the image and the first reference point (`xa,ya`) in pixel coordinates (`xd,yd`). These can be used to scale and translate the mesh to georeference it for small sites.

The latter georeferencing is embedded within the script for the bathymetry interpolation onto the mesh `bath22a` by bookkeeping for each cell a depth value in the vector `hb`. The interpolation of `bath22a` attributes surveyed and remotely sensed depths as per their area share of Voronoi polygons. The composite of survey and remotely sensed bathymetry is shown in

Figure 2.

A string of finite volume cells that bound mangrove nooks, ongoing developments, coverage by marine vessels, or ill-resolved harbor bathymetry can be identified in an index-plot with `plot0(u,v,1:length(u),'mesh.mat','0','-','txt')`, null vectors as dummy velocities, and the visualized quantity, here the indices, being denoted (`'txt'`) in each delineated (`'-'`) cell. The meshing code is not discussed here because the consistency of the output Voronoi diagram can be ascertained visually. The identified boundary of the area to be amended is then denoted in a list of cells (`list_const`) with a constant null concentration (`c_const = 0`) in a simulation's case file (`c(list_const) = c_const`). Any random cell inside a listed area of concern (`list_c0`) can conveniently return via advective propagation all the area's cells as non-zero. That is, the tidal advection simulation is merely exploited to automatically mark the area delineated by `list_const`. Identified cells, that is, a concerned area `area_i = (c>0)`, may be book-kept `save name.mat area_i` and set (`hb(area_i) = `) to the desired depth, in this case, $4m$ for the harbor and $1m$ for the mangrove forest.

3.2 Boundary conditions

Tidal, current, open, and/or other horizontal boundaries are specified by plotting cell indices, with the accordingly configured plotting function, with a zero-order interpolation `plot23(u,v,1:length(u),'mesh.mat','0','-','txt')`. The mesh generator numbers cell indices sequentially along the boundary. Therefore, quantities at the boundary can be set to boundary conditions by referring to a particular boundary section with `index_1:index_2`. For example, in the case of a tidal boundary condition `nodes(1:length(istart:iend)) = istart:iend`.

The bed roughness length was identified, as illustrated in Figure 3, with Equation 52 to specify the bottom boundary condition. The time series of vertical profiles from current meters came with some uncertainties: Occasionally the surface velocity is slower than in lower layers which can occur due to transient dynamics such as wind forcing. The vertical profile spacing from the sea surface, with a top layer of $1.2\,\mathrm{m}$ and other layers of $0.5\,\mathrm{m}$, exhibited cumulative layer thicknesses that occasionally did not match the total measured depth. Therefore, a considerable uncertainty in the layer thickness had to be assumed and a sensitivity study conducted for the same.

Equation 52 can become ill-posed to such uncertainties which will not always average out: If, for example, there is only a minuscule difference between the two velocities in the denominator, then the roughness length is overestimated by logarithmic orders of magnitude. Likewise, the equation is sensitive to an error in height z_1. Consequentially, not the difference between adjacent $0.5\,\mathrm{m}$ thin layers but two layers apart, that is, layer 3 and 5, have been considered. The bottom layer, in principle, would have been more indicative but has been disregarded to obtain a lower relative error for the reference height. Additionally, measurements were excluded that did not exhibit a significant or positive vertical velocity difference $\delta u = u_1 - u_2$.

In order to ascertain a well-posed response despite the uncertainty in reference height and the filtration of small δu, both has been varied and the parameter identification conducted with $2,000$ measurements. The roughness length distribution is shown in Figure 3. Particularly compared to the considerable fluctuations in surface friction, Figure 3 retains well-posedness and returns, regardless of set minimal δ in velocity and assumed reference height, a roughness length on the order of $.2\,\mathrm{m}$. That is, regardless of the two varied parameter, a roughness length on the order of $0.2\,\mathrm{m}$ is obtained.

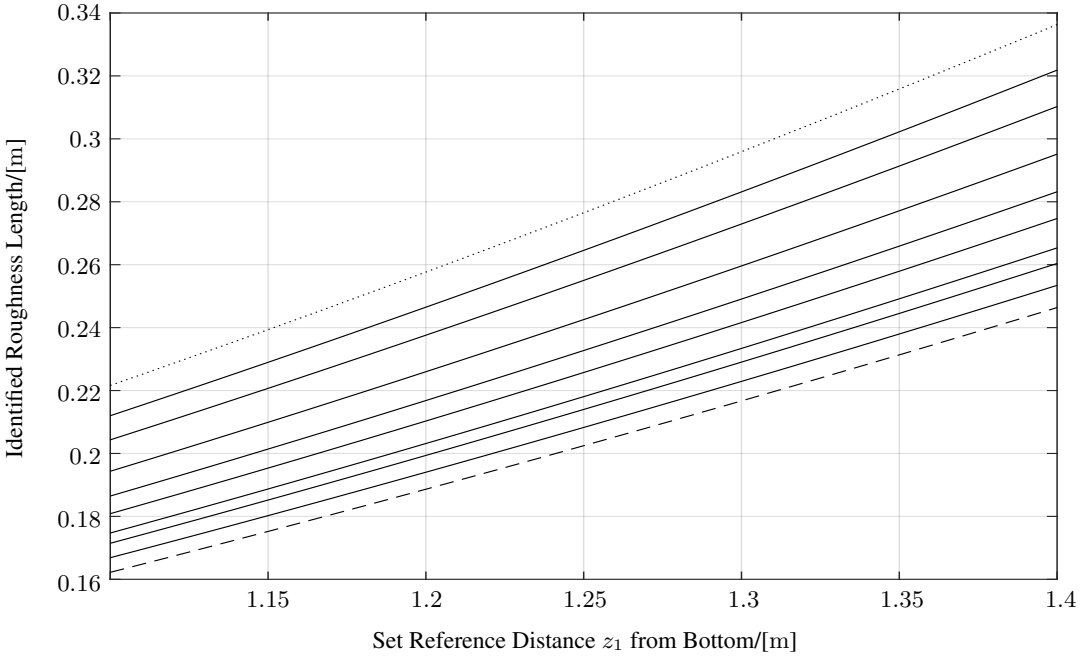

Figure 3. Identified roughness length z_0 vs. varied uncertain reference height $z_1 = 1.25 \pm 0.15\,\mathrm{m}$ and altered minimal velocity difference δu from $1\,\%$ (dashed) to $10\,\%$ (dotted) with ascending one-percent increments in between (solid).

3.3 Validation

Surface elevation predictions have been stored during the simulation for finite volumes that correspond to the tidal and current meter locations within the computational domain. Measured and simulated time series were vertically referenced to the observed mean sea level with `TM = TM - mean(TM)`, correlated, and exhibited the accuracies compiled in Table tab:validity below. For the measured time series, the start time is specified with `t1 = datetime(2022,9,14,12,0,0)` and the end time translocated by `hours(.5)*(length(TM)-1)` with respect to the start time. The resultant time vector is build as per the data point frequency `tTM=t1:hours(.5):t2`, reflective of the half-hourly sampling. The trivial `hold on` command provides for the superposition of the plots for the measured and simulated surface elevation with `plot(tTM,TM)` and so forth.

Surveyed and simulated surface elevations as well as error, mean error and root mean square error (RMSE) are depicted in Figures 4 and 5. Table 3 furthermore contains percent erros besides absolute errors, percent RMSE, as well as R^2 and R-Pearson to quantify the quality of correlation. Two survey locations served to specify the boundary forcing and three survey locations served to validate the accuracy of the simulation. Given that two seasons have been examined, four time series were available for boundary forcing and six to validate the simulation.

Table 3. Validation of Simulated with Measured Surface Elevation. $*$ 0.9957 rounded after third digit.

Quantity	CM2 August	TM2 August	TM3 August	TM2 April	TM3 April
% Error ϵ	1.7	4.8	2.4	5.6	3.8
Abs. ϵ [cm]	3.3	9.4	4.6	8.9	6.0
RMSE [cm]	4.4	12	5.9	10	7.6
% NRMSE	2.3	6.9	3.1	6.5	4.8
R^2	0.99	0.94	0.98	0.94	0.97
R-Pearson	1.0*	0.97	0.99	0.97	0.99

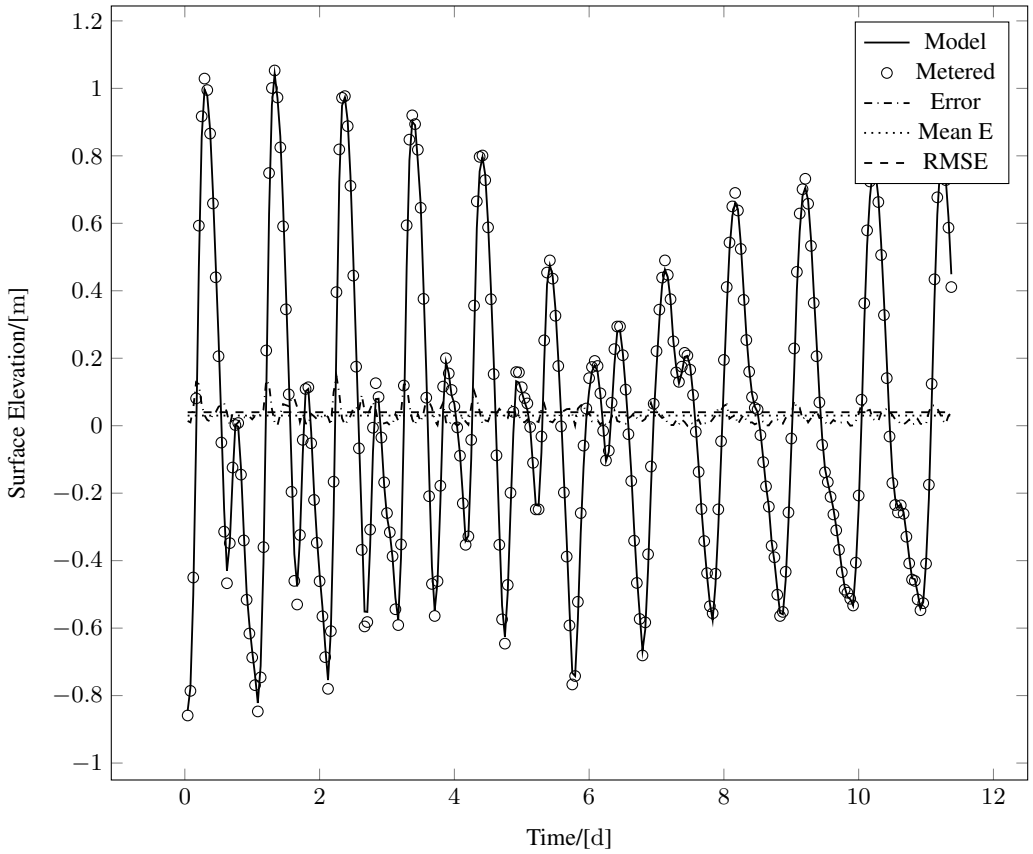

Figure 4. Correlation of simulated and surveyed surface elevation at the location of current meter 2 which also recorded depth, that is, surface elevation in August 2023.

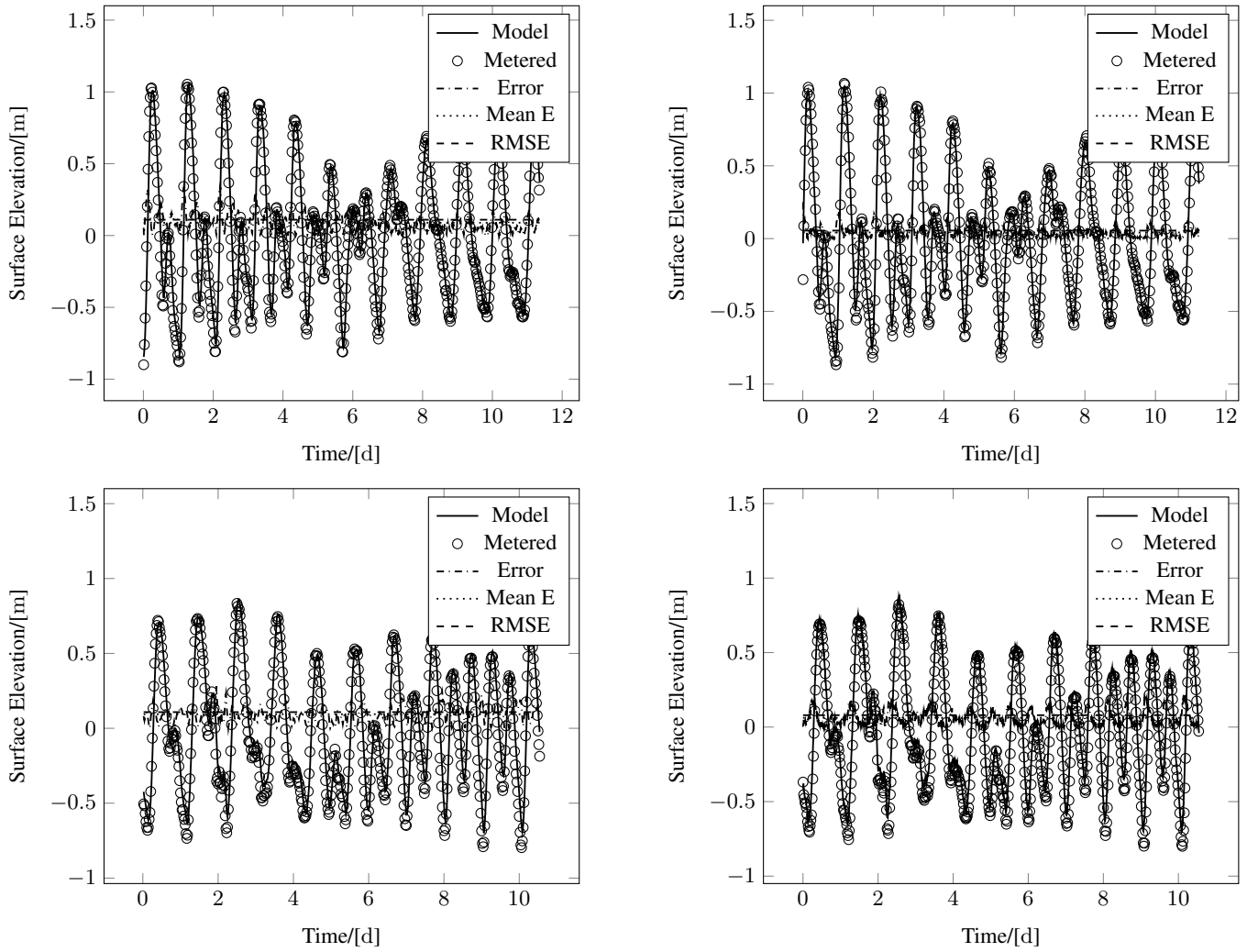

Figure 5. Correlation of simulated and surveyed surface elevation at the location of tidal meter 2 (left) and 3 (right) during August (top) and April (bottom) of 2023.

3.4 Waves, sediment entrainmnt, and settling

460 Wave motion has been resolved with a high resolution mesh for wave propagation with an even resolution throughout the entire domain. High energy waves as per the NOAA CFSR model have been compiled (Wallingford, 2017) for $25.50°$ N, $52.17°$ E, listed in Table 4, and wave transmission been modeled within Doha Bay (Center, 2023). The latter found for the shortest and longest wave period, 6.40 and 7.12 seconds, a transmission to significant wave heights on the order of 0.1 and 0.4 m respectively. The same parameter were simulated with the wave-resolving model in order to resolve wave transmissions for

Katara and account for groyne modifications. The periods of 6.4 and 7.12 s correspond to wavelengths $L = gT^2/(2\pi)$ of 64 and 79 m, which were resolved with the ~ 6 m fine high-resolution mesh.

Table 4. High Energy Wave Conditions East of Safliya Island, NOAA CFSR

Return period /[year]	H_s /[m]	T_p /[s]	Direction /[°]
100	1.92	6.40	12.5
100	2.34	7.12	57.5
100	2.67	6.99	102.5
100	2.05	5.72	147.5

Fine structures, shown in Figure 7, in tidal currents have also been resolved with the high resolution mesh. Both, horizontal geometry and bathymetry, determine the transformation of incoming waves. Acceleration due to continuity at narrow or shallow sections yield an acceleration in both, the depth-averaged and the friction velocity, the latter driving the entrainment of sediment and, hence, erosion.

Second order Stokes waves enter the high resolution domain as depicted for the friction velocity in Figure 8. The boundary of the high resolution domain is aligned with the wave direction (Center, 2023) with the waves being superimposed to the tidal boundary condition. High friction velocity entails erosion. The dynamic friction velocity distribution can, thus, already reveal spots that are vulnerable to morphological changes.

The dynamic Rouse number distribution visualizes where and when sediment settling and erosion predominate since both are time-dependent (Patzke et al., 2022). Values below and above 1 correspond to erosion and settling respectively. Island developments constitute a perturbation of the natural coastal ocean equilibrium in sediment transport. The highly resolved simulation, shown in Figure 9, brings into focus fine pattern and structures, enhancing the reliability of on the former based mitigating measures.

The Rouse number distribution was simulated, resolving wavelengths on the order of 60 m, on a 6 m Voronoi mesh, avoiding wave fronts on acute finite volume polygon angles. The tile pattern exhibited in Figure 6 stems from the 30 m resolution of the open source Landsat satellite images utilized in remote sensing. The mesh has, thus, a higher resolution than the bathymetric model. Nevertheless, commercially available satellite images can facilitate a remote sensing resolution that can match the resolution of the mesh.

A high resolution mesh was produced for Katara beaches with the wave boundary aligned with the wave direction. Currents were simulated for sheltered and high energy conditions and the Rouse number distribution shown for the latter. If the wave's orbital motion does not reach the seafloor, then perturbations of bottom layer currents are small. But waves with wavelengths in excess of the water depth do exert an influence on bottom currents with the latter governing shear and, thus, erosion. Such medium and long wavelength waves can result due to tidal forcing, displayed in Figure 7, as seiches and long wave agitation.

The friction velocity distribution, displayed in Figure 8, and ratio between settling and erosion fluxes, displayed in Figure 9, match previously observed processes: potential for erosion at the southernmost Katara beach and sediment settling at the sheltered beach in the southwest. Sediment settling is found in both, the model and observations, to occur in the sheltered

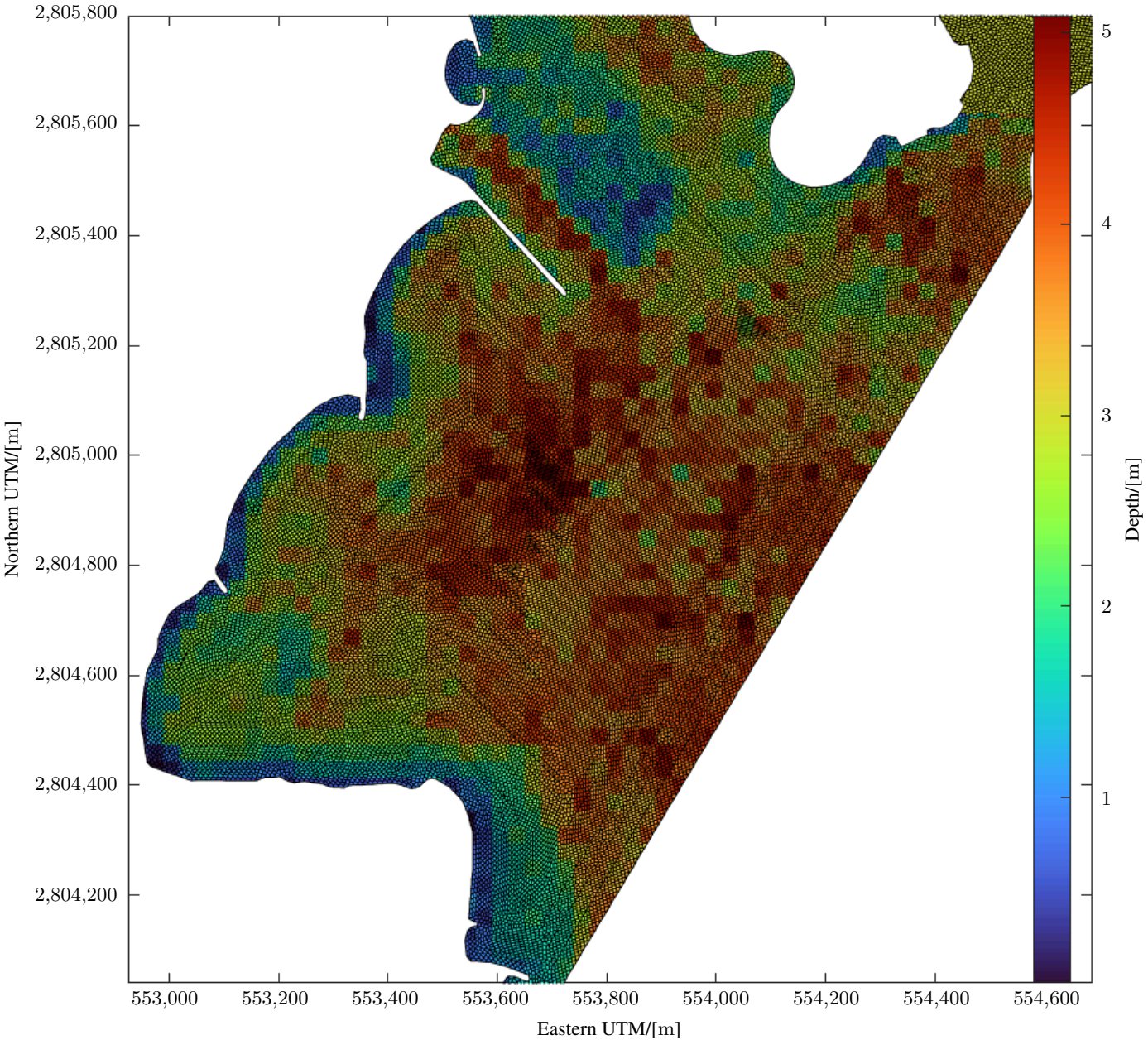

Figure 6. Wave-resolving high resolution mesh to bring into focus the propagation of high energy waves. The northern portion of the mesh is not shown to resolve individual cells in the plot.

southernmost of the three crescent beaches. Erosion is impeded adjacent to recently added groynes. However, for the northern groyne, erosion is impeded only south of it due to the angle of the groyne.

That is, the wave-resolving simulation brought fine patterns into focus that might not be recovered absent the deployed high

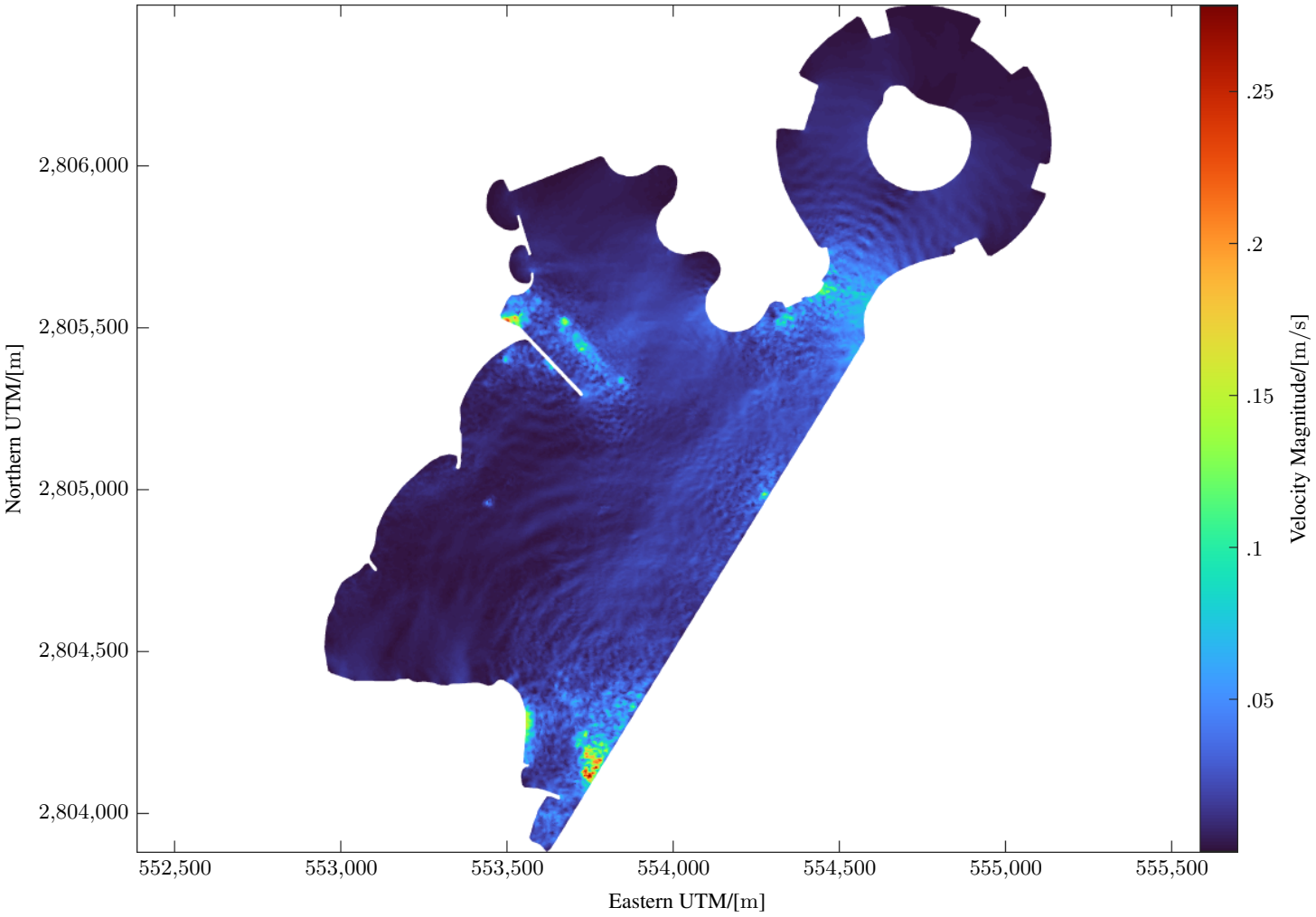

Figure 7. Wave-resolving simulation of tidal regime, showing the velocity magnitude distribution.

resolution, enhancing coastal management. This encourages to conduct sediment transport simulations on Voronoi mesh-based platforms and with high resolution enabled by parallelization or GPU acceleration. The wave-resolving simulation, displayed in Figure 8, resolves wave-driven dynamics that dominate the friction velocity and wave attenuation in the marina north of the development.

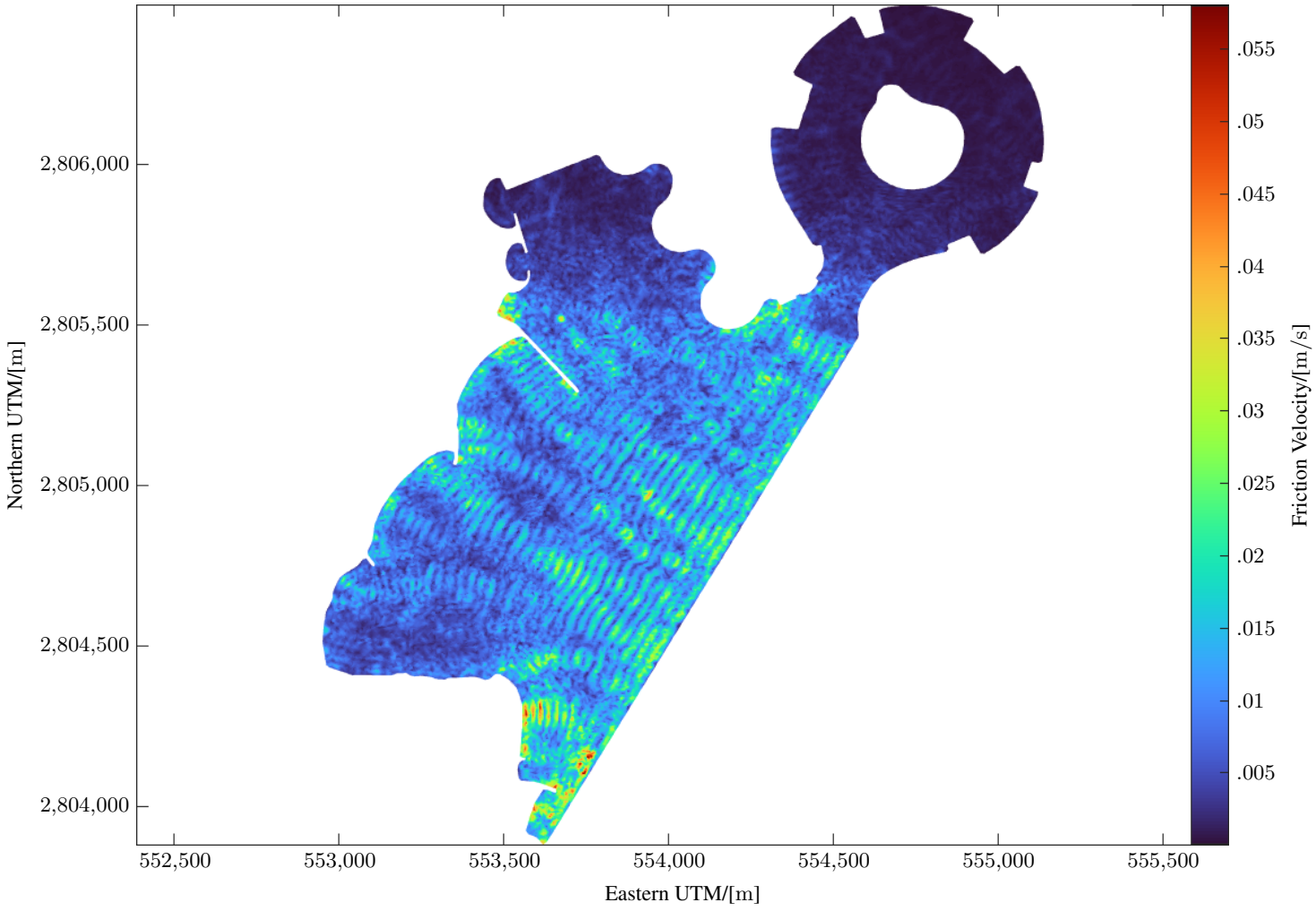

Figure 8. Wave-resolving simulation of high energy regime, showing a moment in time for the dynamic bottom friction velocity distribution. The latter governs erosion.

4 Conclusions

Simulated surface elevations have been validated with five time series from three tidal meters and for two seasons, April and Augsut 2023. The model exceeds real-time performance on a Ryzen 9 or comparable desktop CPU. Vertical current profile data were used to calibrate and conduct a sensitivity study for the roughness length, boundary conditions were set based on two tidal meter, and the validation conducted based on data from three locations, totaling five locations for validation, calibration, and boundary conditions.

The correlation of simulated and surveyed surface elevation time series, exhibited an exceptionally precise correlation, data and simulation being for some plots visually identical, yielding a high confidence in model results. Mean error and RMSE

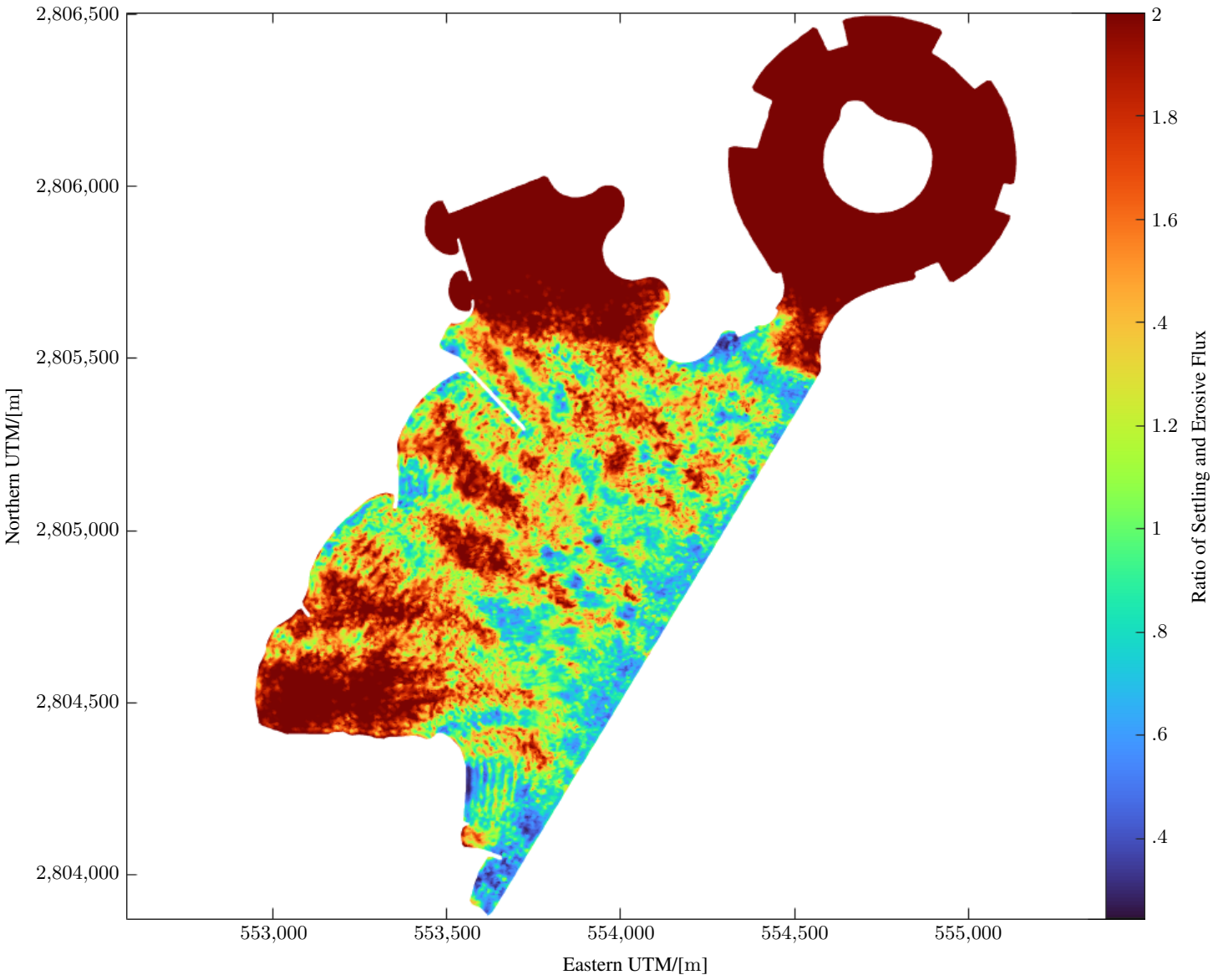

Figure 9. Ratio of sediment settling and erosion fluxes, showing sediment settling at the southern of the three Katara beaches (red), erosion (blue) at the southernmost beach and the functioning of the groynes. The northern groyne that is tilted to the south only shelters its southern side.

were consistently below 7 % as visualized in Figures 4 and 5 as well as compiled in Table 3. With Voronoi-capable models a reduction in cell count, numerical diffusion (Holleman et al., 2013; Chan et al., 2018), and, as demonstrated herein, acute polygon angles can be achieved. The model structure aligns with seamless pre- and post-processing in Matlab as documented in the paper, automatic parallelization, and seamless GPU acceleration. Documented are different approximations for some

terms of the NS PDE, listed in Table 1. These alternatives additionally provide for cross-correlation between different solvers, readily providing a discrepancy-based error estimate for adaptive time stepping.

The model comes with a comprehensive environment of modules, a remote sensing module with spiking neuron filtration, published prior (Lawen et al., 2022), its pollutant fate transport model for nonlinear conversion, published prior (Lawen et al., 2013, 2014), and the Voronoi mesh generator published separately. The simulated, highly resolved dynamic Rouse number distribution, the ratio between sediment settling and erosive flux, displayed in Figure 9, accounts for orbital wave motion. Otherwise unresolved details in settling and erosion, particularly adjacent to the groynes, have been recovered in Figure 9. Wave-resolved simulations can, therefore, considerably enhance coastal management.

Voronoi schemes can be expanded to n dimensions, which might not improve results for coastal systems: the usual approach (Lawen et al., 2010, 2013, 2014) of resolving the vertical rather via multiple layers retains an alignment with the dominant horizontal current components and, thus, avoids numerical diffusion. That is, retaining multiple layers achieves quasi flow alignment for the vertical. This caution might not hold for modeling wave breaking or moving coastal meshes (4D Voronoi). For comprehensiveness, the development of a global model may be a subsequent stage, a step that likewise provides boundary conditions for regional and local models (Holleman and Stacey, 2014; Chou et al., 2015).

References

Anastasiou, S. and Sylaios, G.: Nearshore wave field simulation at the lee of a large island, Ocean Engineering, 74, 61–71, 2013.

Bharadwaj, S. and Sreenivasan, K.: An Introduction to Algorithms in Quantum Computation of Fluid Dynamics, Tech. Rep. STO-EN-AVT-377, NATO Science and Technology Organization, New York, USA, https://www.sto.nato.int/publications/STO%20Educational%20Notes/STO-EN-AVT-377/EN-AVT-377-01.pdf, 2022.

Bleck, R.: An oceanic general circulation model framed in hybrid isopycnic-Cartesian coordinates, Ocean Modelling, 4, 55–88, https://doi.org/https://doi.org/10.1016/S1463-5003(01)00012-9, 2002.

Blumberg, A.: Numerical Tidal Model of Chesapeake Bay, Journal of Hydraulic Engineering, 103, 1–10, 1977.

Center, T. E. C.: WAVES & SEDIMENT MODELLING STUDIES — Katara, Tech. rep., TRUST Engineering Consulting Center, 2023.

Chan, R., Howland, M., Suresh, S. J., and Wienkers, A.: Solution of the 2D Incompressible Navier-Stokes Equations on a Moving Voronoi Mesh, https://web.stanford.edu/~sjsuresh/cfd2017.pdf, 2018.

Chen, C., Beardsley, Geoffrey, R. C. ., Cowles, G., Qi, J., Lai, Z., Gao, G., Stuebe, D., Xu, Q., Xue, P., Ge, J., Ji, R., Hu, S., Tian, R., Huang, H., Wu, L., and Huichan, L.: AN UNSTRUCTURED-GRID, FINITE-VOLUME COMMUNITY OCEAN MODEL FVCOM USER MANUAL (3RD EDITION), http://fvcom.smast.umassd.edu/wp-content/uploads/2013/11/MITSG_12-25.pdf, 2011.

Chou, Y.-J., Holleman, R. C., Fringer, O. B., Stacey, M. T., Monismith, S. G., and Koseff, J. R.: Three-dimensional wave-coupled hydrodynamics modeling in South San Francisco Bay, Comput. Geosci., 85, 10–21, https://doi.org/10.1016/j.cageo.2015.08.010, 2015.

Cousins, B. R., Borne, S. L., Linke, A., Rebholz, L. G., and Wang, Z.: Efficient linear solvers for incompressible flow simulations using Scott-Vogelius finite elements, Numerical Methods for Partial Differential Equations, 29, 1217–1237, https://doi.org/https://doi.org/10.1002/num.21752, 2013.

Faria, A. F. G., Thornton, E. B., Stanton, T. P., Soares, C. V., and Lippmann, T. C.: Vertical profiles of longshore currents and related bed shear stress and bottom roughness, Journal of Geophysical Research: Oceans, 103, 3217–3232, https://doi.org/10.1029/97JC02265, 1998.

Feddersen, F., Gallagher, E., Guza, R., and Elgar, S.: The drag coefficient, bottom roughness, and wave-breaking in the nearshore, Coastal Engineering, 48, 189–195, https://doi.org/10.1016/S0378-3839(03)00026-7, 2003.

Grant, W. D. and Madsen, O. S.: Combined wave and current interaction with a rough bottom, Journal of Geophysical Research: Oceans, 84, 1797–1808, https://doi.org/10.1029/JC084iC04p01797, 1979.

Hallberg, R.: Stable Split Time Stepping Schemes for Large-Scale Ocean Modeling, Journal of Computational Physics, 135, 54–65, https://doi.org/https://doi.org/10.1006/jcph.1997.5734, 1997.

Herzfeld, M., Engwirda, D., and Rizwi, F.: A coastal unstructured model using Voronoi meshes and C-grid staggering, Ocean Modelling, 148, 101 599, https://doi.org/https://doi.org/10.1016/j.ocemod.2020.101599, 2020.

Holleman, R., Fringer, O., and Stacey, M.: Numerical diffusion for flow-aligned unstructured grids with applications to estuarine modeling, Int. J. Numer. Methods Fluids, 72, 1117–1145, https://doi.org/10.1002/fld.3774, 2013.

Holleman, R. C. and Stacey, M. T.: Coupling of Sea Level Rise, Tidal Amplification, and Inundation, Journal of Physical Oceanography, 44, 1439 – 1455, https://doi.org/10.1175/JPO-D-13-0214.1, 2014.

Hsu, M.-H., Kuo, A. Y., Kuo, J.-T., and Liu, W.-C.: Procedure to Calibrate and Verify Numerical Models of Estuarine Hydrodynamics, Journal of Hydraulic Engineering, 125, 166–182, https://doi.org/10.1061/(ASCE)0733-9429(1999)125:2(166), 1999.

Hsu, T.-W., Ou, S.-H., and Liau, J.-M.: Hindcasting nearshore wind waves using a fem code for swan, Coastal Engineering, 52, 177–195, 2005.

Isobe, A. and Beardsley, R. C.: An estimate of the cross-frontal transport at the shelf break of the East China Sea with the Finite Volume Coastal Ocean Model, Journal of Geophysical Research: Oceans, 111, 2005JC003 290, https://doi.org/10.1029/2005JC003290, 2006.

Itani, W. A.: Fluid Dynamicists Need to Add Quantum Mechanics into their Toolbox, https://hal.science/hal-03129398, working paper or preprint, 2021.

Kolmogorov, A. N.: Local structure of turbulence in an incompressible fluid at very high Reynolds numbers, Dokl. Akad. Nauk SSSR, 31, 99–101, 1941.

Kundu, P. K., Cohen, I. M., and Dowling, D. R.: Fluid Mechanics, Elsevier Academic Press, 6 edn., https://www.sciencedirect.com/book/9780124059351/fluid-mechanics, 2016.

Lawen, J.: Solitary solution method for incompressible Navier-Stokes PDE, arXiv preprint arXiv:2104.09183, primary class: math.AP, 2023.

Lawen, J.: Solving the Navier-Stokes PDE with dynamic manifolds: validating numerical solvers for arbitrary geometries, Computational and Mathematical Methods, submitted, 2024.

Lawen, J., Huaming, Y., Linke, P., and Abdel-Wahab, A.: Industrial Water Discharge and Biocide Fate Simulations with Nonlinear Conversion, in: Proceedings of the 2nd Annual Gas Processing Symposium, edited by Benyahia, F. and Eljack, F. T., vol. 2 of *Advances in Gas Processing*, pp. 99–106, Elsevier, Amsterdam, https://doi.org/https://doi.org/10.1016/S1876-0147(10)02011-2, 2010.

Lawen, J., Yu, H., Fieg, G., and Abdel-Wahab, A.: New unstructured mesh water quality model for coastal discharges, Environmental Modelling & Software, 40, 330 – 335, https://doi.org/https://doi.org/10.1016/j.envsoft.2012.08.005, 2013.

Lawen, J., Yu, H., Fieg, G., Abdel-Wahab, A., and Bhatelia, T.: New Unstructured Mesh Water Quality Model for Cooling Water Biocide Discharges, Environmental Modeling & Assessment, 19, 1–17, https://doi.org/10.1007/s10666-013-9370-6, 2014.

Lawen, J., Lawen, K., Salman, G., and Schuster, A.: Multi-Band Bathymetry Mapping with Spiking Neuron Anomaly Detection, Water, 14, https://doi.org/10.3390/w14050810, 2022.

Muin, M. and Spaulding, M.: Two-Dimensional Boundary-Fitted Circulation Model in Spherical Coordinates, Journal of Hydraulic Engineering, 122, 512–521, https://doi.org/10.1061/(ASCE)0733-9429(1996)122:9(512), 1996.

Oey, L.-Y., Mellor, G. L., and Hires, R. I.: A Three-Dimensional Simulation of the Hudson–Raritan Estuary. Part I: Description of the Model and Model Simulations, Journal of Physical Oceanography, 15, 1676–1692, https://doi.org/10.1175/1520-0485(1985)015<1676:ATDSOT>2.0.CO;2, 1985.

on Climate Change, I. P.: Summary for Policymakers, Tech. rep., Contribution of Working Group I to the Fourth Assessment Report of the Intergovernmental Panel on Climate Change, Cambridge, United Kingdom and New York, NY, USA, 2007.

Park, K.: A Vertical Two-Dimensional Model of Estuarine Hydrodynamics and Water Quality, Spec. Rep. App. Mar. Sci. and Ocean Eng. No. 321, Virginia Institute of Marine Science, Gloucester Point, Va., 47, https://doi.org/10.21220/V50F2M, 1993.

Patzke, J., Nehlsen, E., Fröhle, P., and Hesse, R. F.: Spatial and Temporal Variability of Bed Exchange Characteristics of Fine Sediments From the Weser Estuary, Frontiers in Earth Science, 10, https://doi.org/10.3389/feart.2022.916056, 2022.

Ringler, T., Petersen, M., Higdon, R. L., Jacobsen, D., Jones, P. W., and Maltrud, M.: A multi-resolution approach to global ocean modeling, Ocean Modelling, 69, 211–232, https://doi.org/https://doi.org/10.1016/j.ocemod.2013.04.010, 2013.

Skamarock, W. C., Klemp, J. B., Duda, M. G., Fowler, L. D., Park, S.-H., and Ringler, T. D.: A Multiscale Nonhydrostatic Atmospheric Model Using Centroidal Voronoi Tesselations and C-Grid Staggering, Monthly Weather Review, 140, 3090 – 3105, https://doi.org/https://doi.org/10.1175/MWR-D-11-00215.1, 2012.

Smagorinsky, J.: General Circulation Experiments with the Primitive Equations, Monthly Weather Review, 91, 99, https://doi.org/10.1175/1520-0493(1963)091<0099:GCEWTP>2.3.CO;2, 1963.

Tadesse, Y. B. and Fröhle, P.: Modelling of Flood Inundation due to Levee Breaches: Sensitivity of Flood Inundation against Breach Process Parameters, Water, 12, https://doi.org/10.3390/w12123566, 2020.

Wallingford, H.: Doha Port Development, Tech. rep., HR Wallingford, 2017.

Weisberg, R. H. and Zheng, L.: Circulation of Tampa Bay driven by buoyancy, tides, and winds, as simulated using a finite volume coastal ocean model, Journal of Geophysical Research: Oceans, 111, 2005JC003 067, https://doi.org/10.1029/2005JC003067, 2006.

Yang, Z. and Khangaonkar, T.: Modeling the Hydrodynamics of Puget Sound Using a Three-Dimensional Unstructured Finite Volume Coastal Ocean Model, in: Estuarine and Coastal Modeling (2007), pp. 1–17, American Society of Civil Engineers, Newport, Rhode Island, United States, ISBN 9780784409909, https://doi.org/10.1061/40990(324)1, 2008.

Yu, H., Yu, H., Wang, L., Kuang, L., Wang, H., Ding, Y., ichi Ito, S., and Lawen, J.: Tidal propagation and dissipation in the Taiwan Strait, Continental Shelf Research, 136, 57–73, https://doi.org/https://doi.org/10.1016/j.csr.2016.12.006, 2017.

Yu, H., Li, J., Wu, K., Wang, Z., Yu, H., Zhang, S., Hou, Y., and Kelly, R. M.: A global high-resolution ocean wave model improved by assimilating the satellite altimeter significant wave height, International Journal of Applied Earth Observation and Geoinformation, 70, 43–50, 2018.